Origin and K-Ar age of the phreatomagmatic breccia at the Trepča Pb-Zn-Ag skarn deposit, Kosovo: Implications for ore-forming processes

Sabina Strmić Palinkaš[1,*], Ladislav Palinkaš[2], Magda Mandić[3], Zvjezdana Roller-Lutz[4], Zoltan Pécskay[5], Gani Maliqi[6] and Vladimir Bermanec[2]

[1]University of Tromsø, Faculty of Science and Technology, Department of Geology, Dramsvegen 201, N-9037 Tromsø, Norway
(*corresponding author, email: sabina.s.palinkas@uit.no)
[2]University of Zagreb, Faculty of Science, Geological Department, Horvatovac 95, HR-10000 Zagreb, Croatia
[3]Thermo Fisher Scientific, Hanna-Kunath-Straße 11, D-28199 Bremen, Germany
[4]University of Rijeka, Medical Faculty, Department of Physics, Braće Branchetta 20, HR-51 000 Rijeka, Croatia
[5]Institute of Nuclear Research, Hungarian Academy of Sciences, Bemtér 18/C, H-4001 Debrecen, Hungary
[6]Prishtina University, Faculty of Mines and Metallurgy, Mitrovica, Kosovo

121-142 12 Figs. 4 Tabs. doi:10.4154/gc.2016.10

Article history:
Received September 24, 2015
Revised and accepted January 05, 2016
Avaliable online February 29, 2016

ABSTRACT

The Trepča Pb-Zn-Ag skarn deposit in Kosovo is spatially and temporarily related to the phreatomagmatic breccia of Oligocene age (~23Ma). The deposit shows features typical for skarn deposits worldwide, including a stage of isochemical metamorphism, a prograde stage of an anhydrous, low oxygen and low sulfur fugacity character, and a retrograde stage characterized by an increase in the water activity as well as by an increase in oxygen and sulfur fugacities. The mineralization is hosted by the recrystallized Upper Triassic limestone. The prograde mineralization consists mainly of Ca-Fe-Mn±Mg pyroxenes. The host recrystallized limestone at the contact with the prograde (skarn) mineralization has an increased content of Fe, Mn, Mo, As, Au, Cs, Ga, REE and Y suggesting their transport by infiltrating magmatic fluids. The decreased δ^{13}C and δ^{18}O values reflect the contribution of magmatic CO_2. The retrograde mineral assemblage comprises ilvaite, magnetite, arsenopyrite, pyrrhotite, marcasite, pyrite, Ca-Fe-Mn±Mg carbonates and quartz. Hydrothermal ore minerals, mostly galena, sphalerite and pyrite, were deposited contemporaneously with the retrograde stage of the skarn development. Syn-ore and post-ore carbonates reflect the diminishing influence of magmatic CO_2. Syn-ore carbonates are enriched in Fe, Mg, Mn, many chalcophile elements, including Ag, As, Bi, Cd, Cu, Pb, Sb and Zn, as well as in Au, Y and REE. The post-ore stage accompanied the precipitation of a significant amount of Ca-rich carbonates including travertine deposits at the deposit surface.

The phreatomagmatic breccia was developed along a NW dipping contact between the ore bearing recrystallized limestone and the overlying schist. It has an inverted cone shape with vertical extension up to 800 m and a diameter of up to 150 m. The upper part of the diatreme (an underground segment of the phreatomagmatic breccia) is characterized by the presence of a hydrothermally altered rootless quartz-latite dyke surrounded by an unsorted polymict breccia mantle. Despite the alteration processes, the dyke has a preserved porphyritic texture. Partly preserved sanidine, accompanied with a mixture of muscovite and quartz, reflects a near-neutral to weakly acidic environment. The clasts of country rocks and skarn mineralization underwent intense milling and mixing due to repeated magmatic penetrations. Sericitization of the breccia matrix, locally accompanied with minor kaolinitization, point to an increased water activity under near-neutral to weakly acidic conditions. Large fragments originally composed of anhydrous skarn minerals (pyroxenes) are usually completely altered to a mixture of fibroradial magnetite, quartz and various amounts of carbonates suggesting an increase in oxygen fugacity. Their pyrite rims reflect that the increase in oxygen fugacity was followed by an increase in sulfur fugacity. The clast predominantly composed of Fe-sulfides and minor Bi-sulfides suggest that the increase in sulfur fugacity was locally sufficient to complete sulfidation of hedenbergite to pyrrhotite and/or pyrite.

Although the phreatomagmatic breccia at the Trepča Pb-Zn-Ag skarn deposit does not carry significant amounts of ore mineralization, its formation was crucial for ore deposition. Phreatomagmatic explosions and formation of the breccia turned the system from the lithostatic to hydrostatic regime and triggered the retrograde stage increasing the water activity and oxygen fugacity in the system. In addition, cooling and decompression of the system contributed to more effective degassing of magmatic sulfur and increased the sulfur fugacity.

Keywords: phreatomagmatic breccia, Pb-Zn-Ag skarn deposit, transition from lithostatic to hydrostatic regime, fluid inclusions, stable isotopes, K/Ar dating

1. INTRODUCTION

Breccia pipes have been recognized in different types of ore deposits, from porphyry to epithermal in their origin (e.g. the Acupan Au-Ag-Te epithermal deposit, Philippines (COOKE & BLOOM, 1990); the Roşia Montană Au-Ag epithermal deposit, Romania (WALLIER et al., 2006); the Cerro de Pasco epithermal polymetallic deposit, Peru (BAUMGARTNER et al., 2008); the El Teniente Cu-Mo porphyry deposit, Chile (CANNELL et al., 2005; VRY et al., 2010)). At some localities a genetic link between the breccia formation and ore mineralization is evident (e.g. the Wau Au deposit, Papua New Guinea (SILLITOE et al., 1984); the Kelian Au deposit, Indonesia (DAVIES et al., 2008); the Galore Creek Cu-Au deposit, British Columbia, Canada (BYRNE & TOSDAL, 2014)), while at others it is more obscure. Also, at some localities breccia pipes host significant amounts of ore (e.g. the Au-bearing breccia pipe at Kidston, Queensland, Australia (BAKER & ANDREW, 1991); the Cu-bearing Donoso breccia pipe, Chile (SKEWES et al., 2003); the base metal-bearing breccia pipe at the Cerro de Pasco deposit, Peru (BAUMGARTNER et al., 2008)) whereas elsewhere they are mostly barren (the Aguablanca Ni-Cu magmatic deposit, Spain (TORNOS et al., 2001); the Copper Creek mining district, Arizona, USA (ANDERSON et al., 2009); the Blackbird Co-Cu-Au-Bi-Y-REE district, Idaho, USA (TRUMBULL et al., 2011)).

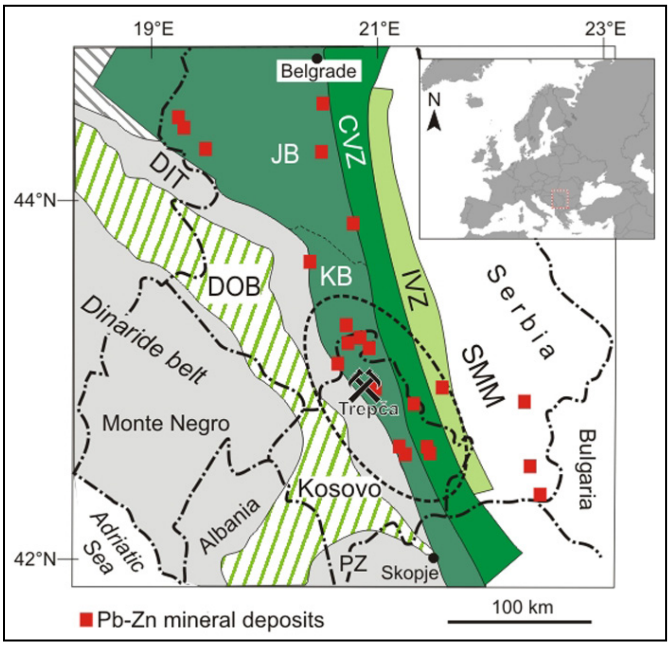

Figure 1. Geological setting of the Pb-Zn mineral deposits, including the Trepča Pb-Zn-Ag skarn deposit, within the Vardar zone, SE Europe (simplified after KARAMATA et al. (2000) and DIMITRIJEVIĆ (2001)). External Vardar Zone: JB – Jadar Block and KB - Kopaonik Block; CVZ - Central Vardar Zone; IVZ - Internal Vardar Zone; DOB – Dinaride Ophiolite Belt; DIT – Drina-Ivanjica Terrain; PZ - Pelagonian Zone; SMM - Serbo-Macedonian Massif.

The Trepča deposit in Kosovo (Fig. 1) is an example of the Pb-Zn-Ag skarn deposit spatially and temporarily related to the phreatomagmatic breccia (STRMIĆ PALINKAŠ et al., 2007; FÉRAUD et al., 2007; STRMIĆ PALINKAŠ et al, 2013). The deposit, with current reserves of 31 Mt of ore at 4.2 % of Pb, 3 % of Zn and 86 g/t of Ag, together with the past production of approximately 34 Mt of ore, represents an important source of metals in the SE part of Europe. A nearly circular breccia pipe occurs at the contact between the mineralized recrystallized limestone of Upper Triassic age and the barren schist (Fig. 2). Although the breccia does not host an economically significant amount of ore, we argue that the mechanism of its formation is a key factor for understanding ore forming processes in the Trepča deposit. The abandoned open pit and the active underground mine expose the breccia over a vertical interval of 800 m and allow access to various breccia lithofacies.

The major aim of this study is to understand the origin of the phreatomagmatic breccia and its role in the ore-deposition processes at the Trepča Pb-Zn-Ag skarn deposit. The study combines descriptive features, mineralogy, stable isotope and fluid inclusion data obtained from the breccia and wall rocks. The K/Ar data gained on whole rock and single grain separates revealed the age of the brecciation event.

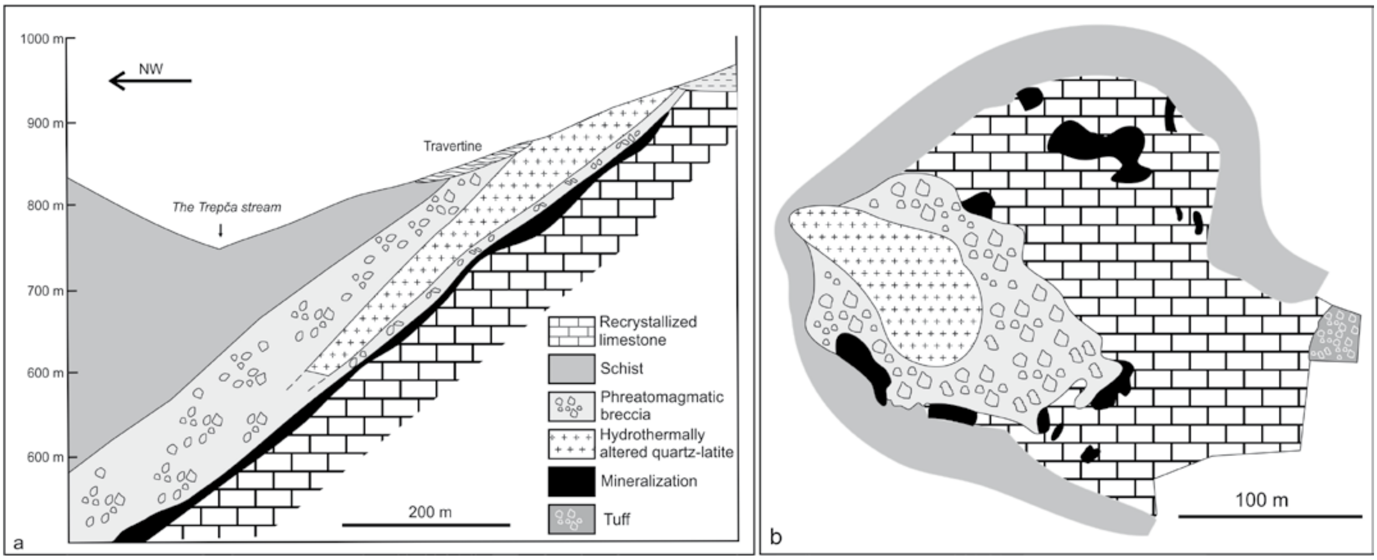

Figure 2. a. Cross section through the Trepča Pb-Zn-Ag skarn deposit; b. Local geological map of the Trepča Pb-Zn-Ag skarn deposit (after SCHUMACHER, 1950).

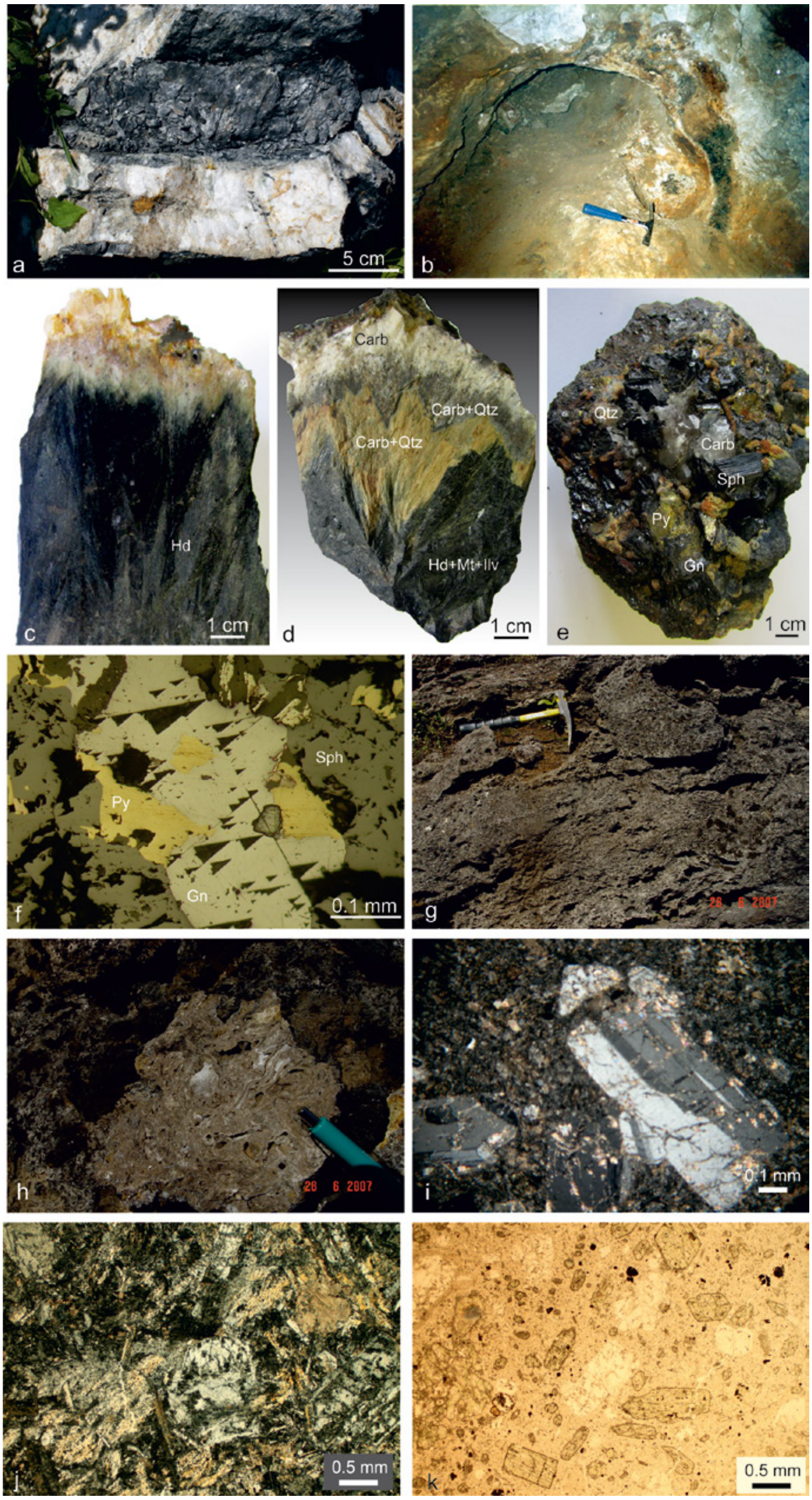

Figure 3. a. Upper Palaeozoic schist intercalated with quartzite layers; b. Recrystallized Upper Triassic limestone with developed karst phenomena; c. Prograde skarn mineralization consisting mainly of pyroxenes; d. Retrograde skarn mineralization comprising a mixture of ilvaite, magnetite, quartz and Ca-Fe-Mn-Mg carbonates; e. Hydrothermal mineralization comprising ore (galena, sphalerite, pyrite) and gangue (carbonate, quartz) minerals; f. The principal ore minerals, galena and sphalerite, are accompanied by various amounts of pyrite; g. Travertine deposits at the surface of the Trepča Pb-Zn-Ag skarn deposit (835 m above mean sea level); h. Close view of the travertine deposit; i. Photomicrographs of trachyte with typical porphyritic texture and altered sanidine phenocrysts (under crossed polarizers); j. Photomicrographs of quartz-latite with altered sanidine, plagioclases, amphiboles and quartz as principal phenocrysts (under crossed polarizers); k. Photomicrographs of andesite composed of plagioclase, amphiboles and quartz phenocrysts embedded within a carbonized and silificated aphanitic groundmass. Mineral abbreviations: Hd – hedenbergite; Mt – magnetite, Ilv – ilvaite; Carb – Ca-Fe-Mn-Mg carbonates; Qtz – quartz; Sph – sphalerite; Gn – galena; Py – pyrite.

2. GEOLOGICAL SETTING

The Trepča Pb-Zn-Ag skarn deposit is situated in the western part of the NW-SE trending Vardar zone that extends throughout the western part of the Balkan Peninsula between the Dinarides, the Drina-Ivanjica Terrain and the Pelagonian Zone to the west and the Serbo-Macedonian Massif to the east (Fig. 1). The Vardar zone represents the main suture zone along the contact between the Adriatic and the Euroasian plate with elements of both continental and oceanic lithologies (DIMITRIJEVIĆ, 2001; KARAMATA et al., 2000; ZELIĆ et al., 2010; ROBERTSON et al., 2013).

During the Late Permian to Middle Triassic the incipient rifting process affected metamorphosed Precambrian-Palaeozoic terrains separating the Pelagonian Zone and the Serbo-Macedonian Massif. Rifting was followed by the development of a subsiding carbonate platform and formation of an oceanic crust during Late Triassic-Early Jurassic time (SHARP & ROBERTSON, 2006; DILEK et al., 2007; ROBERTSON et al., 2013). The Western (External) Vardar Zone represents a complex zone that comprises ophiolites and ophiolitic mélange (KARAMATA et al., 1980). At several localities ophiolitic masses, composed of spinel lherzolite, harzburgite and dunite, have preserved evidence for metamorphic soles at their bases. The K/Ar age between 160 and 123 Ma (KARAMATA et al., 2000; MILOVANOVIĆ et al., 1995) and Ar/Ar age between 175 and 170 Ma (BOROJEVIĆ ŠOŠTARIĆ et al., 2014) obtained from the metamorphic soles suggest emplacement of ophiolites from the Middle Jurassic to the Early Cretaceous. The Jurassic-Cretaceous mélange of the Western Vardar Zone comprises mostly large blocks and fragments of Middle to Upper Triassic and Upper Jurassic limestones, terrigenous sediments (sandstone, greywacke), basalts, and

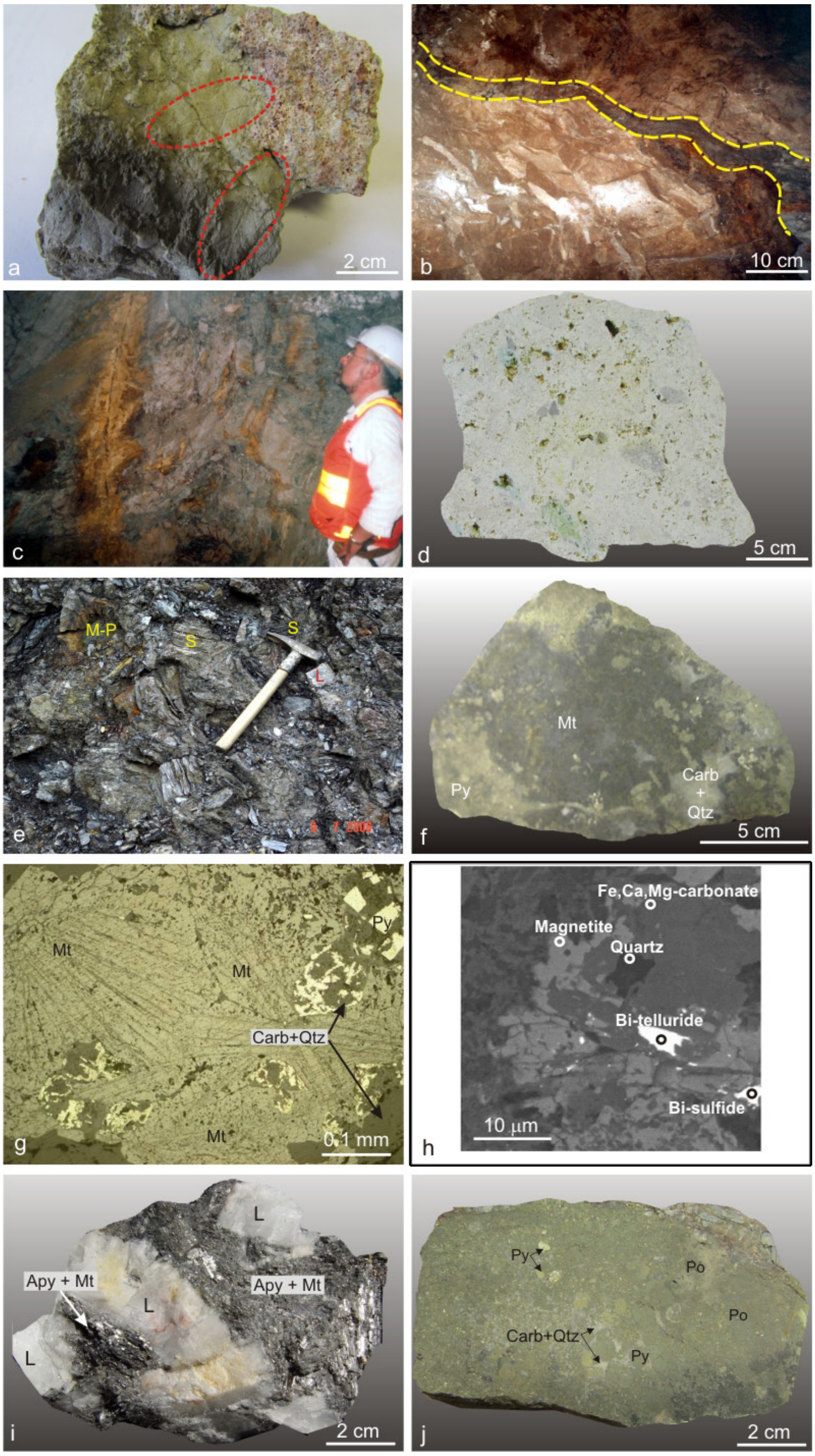

Figure 4. a. Pyroclastic rocks enclose euhedral calcite crystals, fragments of the country rocks and spheroid pumice lapillus. The leaves and plant root traces are also visible; b. Lateral dyke-like branches of the main breccia pipe sporadically intrude the recrystallized Upper Triassic limestone; c. A gradual transition from the main breccia pipe into the brecciated schist; d. Hydrothermally altered quartz-latite from the core of the main breccia pipe. White fine-grained matrix incorporates yellowish to greenish remains of sanidine phenocrysts, quartz phenocrysts and fragments of country rocks, predominantly the schist; e. Randomly oriented fragments of schist (S), recrystallized limestone (L) and magnetite- and pyrite-bearing clasts (M-P), the main breccia pipe, surface (835 m above mean sea level); f. Close view of the clast composed of a magnetite core and pyritic rim; g. Photomicrographs of the clast composed of a fibroradial magnetite core and pyritic rim (plane-polarized light); h. Scanning electron photomicrograph of the clast composed of a magnetite core and pyritic rim reveals the presence of Bi-telluride and Bi-sulfide; i. Recrystallized limestone (L) fragment partly replaced with fibroradial arsenopyrite and magnetite (75 m above mean sea level); j. The clast composed of pyrite, pyrrhotite and minor Bi-sulfides. Mineral abbreviations: Mt – magnetite; Py – pyrite; Po – pyrrhotite, Apy – arsenopyrite; Carb – Ca-Fe-Mn-Mg carbonates; Qtz – quartz.

cherts with Carnian to Norian and Upper Jurassic radiolarians emplaced within an argillaceous to silty matrix (SUDAR & KOVACS, 2006; VASKOVIĆ & MATOVIĆ, 2010). In contrast, the Eastern (Internal) Vardar Zone comprises the weakly metamorphosed mélange of Jurassic age with predominantly basaltic fragments (SUDAR & KOVACS, 2006, and references therein).

The postcollisional magmatism of Oligocene to Miocene age (CVETKOVIĆ et al., 2004) was accompanied by widespread hydrothermal activity in the Western Vardar Zone, producing numerous skarn, hydrothermal replacement and vein type Pb-Zn-Ag deposits (Fig. 1; JANKOVIĆ, 1995; VESELINOVIĆ-WILLIAMS, 2011; BOROJEVIĆ ŠOŠTARIĆ et al., 2013; STRMIĆ PALINKAŠ et al., 2013). The Oligocene to Miocene magmatic rocks is represented mostly by trachytes, quartz-latites, andesites and pyroclastic deposits (CVETKOVIĆ et al., 2004; BOROJEVIĆ ŠOŠTARIĆ et al., 2012).

2.1. GEOLOGY OF THE DEPOSIT

The basement of the Trepča Pb-Zn-Ag skarn deposit comprises a metamorphosed and folded Upper Palaeozoic to Triassic sedimentary complex composed predominantly of schist and recrystallized limestone. The dark coloured schist occasionally is intercalated with compact dense to coarse-grained quartzite layers (Fig. 3a). At the contact with the mineralization the schist is enriched in quartz and micas. The recrystallized limestone frequently exhibits developed karst phenomena (Fig. 3b). The size of calcite grains varies from several millimetres at places spatially distal to the mineralization up to several centimeters along the contact with the ore bodies and the breccia pipe. According to the data obtained from conodont remains the limestone has been assigned to the Upper

Triassic (SUDAR, 1986). The limestone-schist contact is marked by the presence of the breccia pipe (SCHUMACHER, 1950, 1954; FÉRAUD et al., 2007; STRMIĆ PALINKAŠ et al., 2013).

The mineralization of the Trepča Pb-Zn-Ag skarn deposit is exclusively hosted by the recrystallized limestone (Fig. 2). The principal skarn minerals in the Trepča deposit are Ca-Fe-Mn±Mg silicates including pyroxenes, ilvaite and minor garnets. Accessory minerals are Ca-Fe-Mn±Mg carbonates and quartz. Paragenetic studies based on macro- and microtextures show that the skarn assemblage from the Trepča deposit was formed in several stages, similar to other skarns (MEINERT, 1992; MALO et al., 2000; MEINERT et al., 2005; CANET et al, 2011). The prograde stage has an anhydrous character with Ca-Fe-Mn±Mg pyroxenes as the major minerals (Fig. 3c). Ca-Fe garnets (andradite) occur rarely, exclusively in the uppermost levels of the deposit. The retrograde stage has a predominantly hydrous character with ilvaite, magnetite, carbonate and quartz as important products (Fig. 3d). The hydrothermal ore minerals commonly overprint the pyroxene-rich calcic skarn, although skarn mineralization free of the ore assemblage as well as the ore mineralization without skarn precursor has been found (Fig. 3e). Black coloured sphalerite, galena and pyrite are the most abundant sulfide minerals (Fig. 3f). The deposit contains volumetrically minor, but mineralogically diverse Bi-bearing minerals, including native Bi, bismuthinite (Bi_2S_3), cosalite ($Pb_2Bi_2S_5$), cannizzarite ($Pb_4Bi_6S_{13}$), lillianite ($Pb_3Bi_2S_6$), ikunolite ($Bi_4(S,Se)_3$), babkinite ($Pb_2Bi_2(S,Se)_3$), joseite ($Bi_4(S,Te)_3$), heyrovskyite ($Pb_{10}AgBi_5S_{18}$) andizoklakeite ($Pb_{27}(Cu,Fe)_2(Sb,Bi)_{19}S_{57}$) (TERZIĆ et al., 1974; KOŁODZIEJCZYK et al., 2015). Travertine deposits locally occur as a top layer capping the deposit and marking the preserved palaeosurface (Figs. 3g, h).

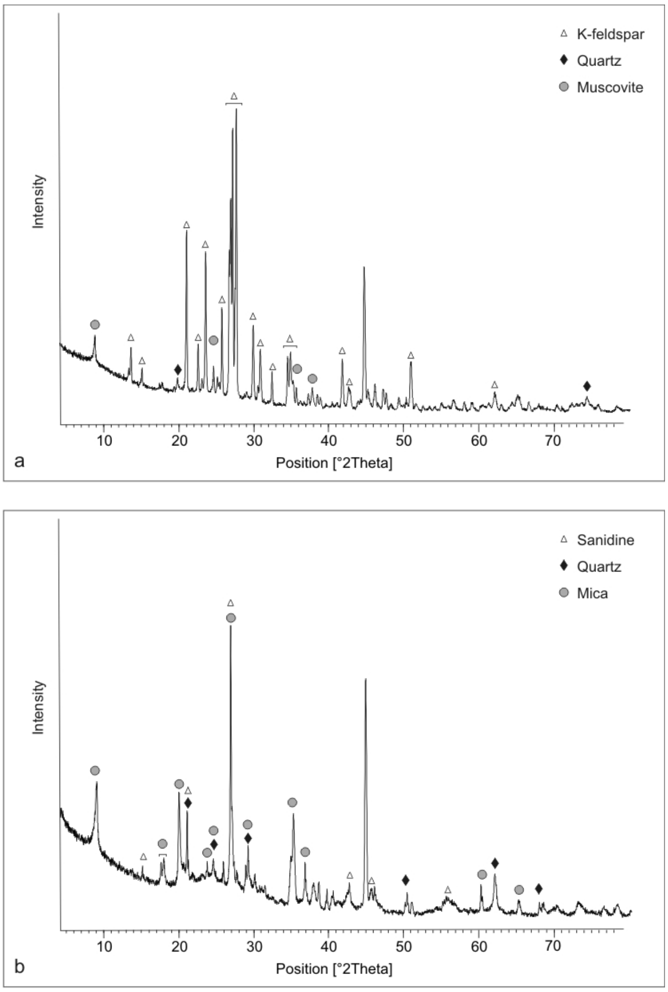

Figure 5. X-ray diffraction patterns reveal that a. hydrothermally altered quartz-latite matrix consists of K-feldspar, quartz and muscovite; b. altered phenocrysts comprise sanidine remains as well as various micas and quartz.

During the Oligocene-Miocene, the Trepča area was a location of considerable volcanicactivity characterized by numerous lava flows and large masses of volcanoclastic rocks. The volcanic rocks are represented mostly by trachytes, quartz-latites and andesites. Trachytes are composed of a light gray matrix and sanidine phenocrysts (Fig. 3i). Quartz-latites are exposed at the Zvečan hill and occur as the core of the breccia pipe within the deposit. Beside sanidine they comprise significant amounts of quartz grains (Fig. 3j). The Ar/Ar age of the Zvečan hill quartz-latite spans between 24.8±0.2 Ma for K-feldspar and 25.8±0.3 Ma for amphibole (BOROJEVIĆ ŠOŠTARIĆ et al., 2012). Andesites are mainly light to medium gray in colour and porphyritic in texture. They are composed of plagioclase, hornblende, biotite, augite and bronzite (Fig. 3k).

2.2 THE BRECCIA GEOMETRY, COMPOSITION AND INTERNAL ORGANIZATION

The breccia pipe exposed at the Trepča Pb-Zn-Ag skarn has an inverted cone shape characteristic for phreatomagmatic breccias elsewhere (e.g. SILLITOE, 1985; TAMAS & MILESI, 2002; LANDTWING et al., 2002; DAVIES et al., 2008). The diatreme (an underground segment of the phreatomagmatic breccia; LORENZ, 1973) extends vertically up to 800 m below the surface and has a diameter of approximately 150 m (Fig. 2). The partly preserved maar structure (a surface expression of phreatomagmatic breccia; LORENZ, 1973) comprises tuffaceous (Fig. 2; SCHUMACHER, 1950) and pyroclastic deposits with common remnants of plant leaves and roots (Fig. 4a). The breccia pipe was emplaced along a NW dipping contact between the ore bearing recrystallized limestone and the overlying schist (Fig. 2). Contacts between the breccia and the recrystallized limestone are mostly sharp but locally cut by lateral dyke-like branches (Fig. 4b) infilled with rock flour ("milled matrix fluidized breccia") or with angular fragments ("jigsaw-puzzle breccia"). In contrast, the contacts with the overlying schist are unclear, with a gradual transition from the breccia pipe into the brecciated schist (Fig. 4c). The upper part of the diatreme hosts a hydrothermally altered quartz-latite dyke with the preserved porphyritic texture (Fig. 4d). The white fine-grained matrix comprises muscovite, quartz, and K-feldspars (Fig. 5). The sanidine phenocrysts are partly altered to a yellowish to greenish fine-grained mixture of muscovite and quartz (Fig. 5). The quartz phenocrysts are well preserved. Fragments of county rocks, especially schist, are embedded within the matrix too. The dyke occupies the pipe core and is surrounded by the unsorted polymict breccia mantle (Figs. 2, 4e).

Table 1. Analyzed samples from the Trepča Pb-Zn-Ag skarn deposit.

Sample	Level	Depth (m a.m.s.l.*)	Description
KM-10	surface	835	host limestone, barren, recrystallized
P1	surface	835	pyroclastic deposit
P2	surface	835	pyroclastic deposit
P4	surface	835	travertine deposit
TR-6	surface	835	quartz-latite
TR-108	surface	835	hydrothermally altered quartz-latite core of the main breccia pipe
KM7-1	surface	835	fragment composed of a magnetite core and a pyrite rim, the main breccia pipe
KM8	surface	835	fragment composed of a magnetite core and a pyrite rim, the main breccia pipe
KM9	surface	835	fragment composed of fractured pyrite, pyrrhotite and minor Bi-sulfides, the main breccia pipe
TR-V-1	V	375	hydrothermal paragenesis
TR-VII-7	VII	255	hydrothermal paragenesis
TR-VIII-2	VIII	195	hydrothermal paragenesis
TR-VIII-4	VIII	195	hydrothermal paragenesis
T8	IX	135	hydrothermal paragenesis
T8a	IX	135	hydrothermal paragenesis
T8-2	IX	135	hydrothermal paragenesis
STS-0	X	75	host limestone, barren, recrystallized
STS-1	X	75	hydrothermal paragenesis
STS-2	X	75	hydrothermal paragenesis
STS-3	X	75	hydrothermal paragenesis
T1	X	75	clast composed of siderite, quartz and dickite, the main breccia pipe
T2	X	75	recrystallized limestone fragment, the main breccia pipe
T2	X	75	recrystallized limestone fragment partly replaced by magnetite and aresenopyrite, the main breccia pipe
T3	X	75	the recrystallized limestone in contact with the main breccia pipe
T3a	X	75	the recrystallized limestone in contact with the main breccia pipe
T4	X	75	recrystallized limestone at the contact with lateral breccia branches
T4a	X	75	lateral breccia branch
T5	X	75	hydrothermal paragenesis
T6a	X	75	skarn paragenesis
T6b	X	75	skarn paragenesis
T6c	X	75	skarn paragenesis
T6d	X	75	skarn paragenesis
T6e	X	75	skarn paragenesis
T6f	X	75	host limestone, barren, recrystallized
T7-2	X	75	hydrothermal paragenesis
T7-3a	X	75	hydrothermal paragenesis
T7-4	X	75	recrystallized limestone at the contact with lateral breccia branches
T7-4a	X	75	lateral breccia branch
T7-5	X	75	hydrothermal paragenesis
T9-1	X	75	skarn paragenesis
T9-3	X	75	skarn paragenesis
T9-4	X	75	skarn paragenesis
T9-5	X	75	hydrothermal paragenesis
T9-6	X	75	skarn paragenesis
148A	X	75	hydrothermal paragenesis
TR-XI-2	XI	15	hydrothermal paragenesis
TR-XI-3	XI	15	hydrothermal paragenesis
TR-XI-4	XI	15	hydrothermal paragenesis
TR-XI-5	XI	15	hydrothermal paragenesis
TR-XI-6	XI	15	hydrothermal paragenesis

* a.m.s.l. – above mean sea level

* a.m.s.l. – above mean sea level

Clasts are angular to well-rounded ranging in size from less than a millimetre to several metres with no systematic distribution in fragment size and roundness. They occupy up to 90 vol.% of the breccia. Fragments of the country rocks, limestones and schists, together with Ca-Fe-Mn±Mg silicate-, magnetite- and sulfide-bearing fragments represent the principal types of clasts. The upper portion of the diatreme is characterized by the extreme mixing of the rock fragments of various origin but besides the country rock fragments, the fragments composed of the magnetite core and pyrite-enriched rim are the most frequent. Magnetite occurs in the form of fibroradial to spherulitic aggregates (Fig. 4f) with minor masses of pyrite, Bi-sulfides, Bi-tellurides, carbonates and quartz emplaced between magnetite grains (Figs. 4g, h). The rim comprises fresh pyrite accompanied by carbonates and quartz (Figs. 4f, g). Fragments of pyroclastic rocks and fragments with lacustrine plant remains have been found at various depths suggesting collapse events (McCALLUM, 1985; BAKER et al., 1986).

In the deeper part of the breccia pipe, magnetite and overprinting fibroradial arsenopyrite are found to be embedded within recrystallized limestone fragments (Fig. 4i). The clasts composed of fractured pyrite, pyrrhotite and minor Bi-sulfides are common at various depths of the breccia pipe. The space between sulfide grains is filled with a fine-grained mixture of carbonates and quartz (Fig. 4j). Quartz-latite (juvenile) fragments occur as well. The breccia matrix comprises a fine-grained rock flour that has been affected by various types of hydrothermal alterations, including sericitization, kaolinitization, pyritization and carbonatization.

3. SAMPLES AND METHODS

A total of forty-nine hand-picked rock samples were collected from existing underground works and from the surface of the Trepča Pb-Zn-Ag skarn deposit. We sampled various types of breccia fragments, wall rocks as well as mineral parageneses (Table 1).

Paragenetic relationships were studied in thin sections by transmitted polarized light microscopy. Ore minerals were examined in polished thick sections by reflected light microscopy. X-ray powder diffraction (XRD) analysis was conducted at the University of Zagreb on a Philips PW 3040/60 X'Pert PRO powder diffractometer (45 kV, 40 μA), with CuKα-monochromatized radiation (λ = 1.54056 Å) and θ-θ geometry. The area between 4 and 63° 2θ, with 0.02° steps, was measured with a 0.5° primary beam divergence. Compound identifications were based on a computer program X'Pert high score 1.0B and literature data. The textural features and semi-quantitative analyses of breccia fragments were examined by a Tescan Scanning Electron Microscope (SEM) equipped with an INCA 250 analyzing system and Oxford detectors at the University of Zagreb. The analyses were performed on carbon-coated polished thin sections using the following operating conditions: 3-40 mm beam, accelerating voltage 20 kV, current 10 nA and counting time of 200 seconds. Bulk chemical compositions of 14 selected samples were prepared in an agate ball mill and analyzed at Acme Analytical Laboratories (Vancouver, Canada) after lithium metaborate or tetraborate fusion using inductively coupled plasma (ICP) for major elements and inductively coupled plasma-mass spectrometry (ICP-MS) for trace elements.

Microthermometric measurements of fluid inclusions within transparent minerals (calcite, quartz) were performed at the University of Zagreb. Double polished, ~0.5-mm-thick, transparent mineral wafers were used. Measurements were carried out on a Linkam THMS 600 stage mounted on an Olympus BX 51 microscope using 10× and 50× Olympus long-working distance objectives for visible light. Two synthetic fluid inclusion standards (SYN FLINC; pure H_2O and mixed H_2O-CO_2) were used to calibrate the equipment. The precision of the system was ±2.0°C for homogenization temperatures, and ±0.2°C in the temperature range between –60° and +10°C. Microthermometric measurements were made on carefully defined fluid inclusion assemblages, representing groups of inclusions that were trapped simultaneously. The fluid inclusion assemblages were identified based on petrography prior to heating and freezing. If all of the fluid inclusions within the assemblage showed similar homogenization temperatures, the inclusions were assumed to have trapped the same fluid and to have not been modified by leakage or necking; these fluid inclusions thus record the original trapping conditions (GOLDSTEIN & REYNOLDS, 1994; GOLDSTEIN, 2001; BODNAR, 2003).

Carbon and oxygen isotope analyses of carbonates from the wall rocks and breccia fragments as well as analyses of carbonates associated with the ore mineralization were performed at the University of Rijeka. Carbonate powder was extracted from hand-picked samples using a dentist's drill. A mass of 250 μg of powder has been loaded in sealed reaction vessels, then flushed with helium gas and reacted at 72°C with phosphoric acid. The evolved carbon dioxide was sampled using a Thermo Finnigan Gas-Bench and isotope ratios were measured in continuous flow mode using a Thermo Finnigan Delta^{plus} XPmass spectrometer. The data was extracted into an EXCEL file by using the ISODAT NT EXCEL export utility and further calculation steps were carried out using a predefined EXCEL worksheet. Linearity corrections were ap-

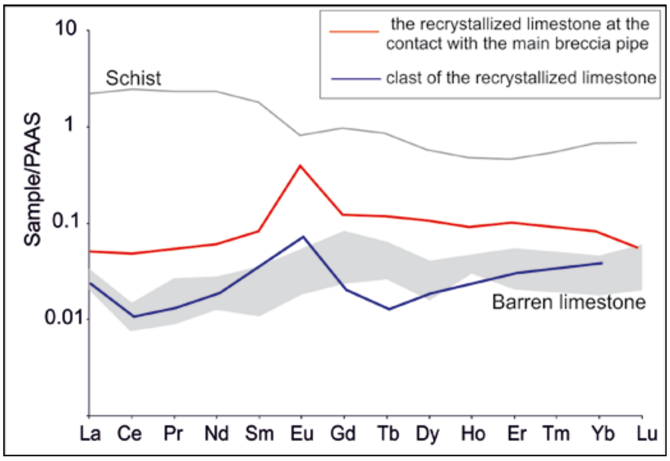

Figure 6. The post-Archean Australian shale (PAAS) normalized plots of the recrystallized limestone at the contact with the main breccia pipe and the recrystallized limestone clast from the main breccia pipe (75 m above mean sea level). The data for the schist and barren limestone are adopted from STRMIĆ PALINKAŠ et al. (2013).

Table 2. Chemical composition of carbonates from the Trepča Pb-Zn-Ag skarn deposit.

		SiO_2	Al_2O_3	Fe_2O_3	MgO	CaO	Na_2O	K_2O	TiO_2	P_2O_5	MnO	Cr_2O_3
						%		ppm				
Barren recrystallized limestone												
STS-0*	Recrystallized limestone	0.22	0.07	0.07	0.41	55.69	0.01	0.04	0.01	0.01	0.01	0.001
KM10*	Recrystallized limestone	0.13	0.03	0.07	0.08	56.77	0.01	0.04	0.01	0.01	0.03	0.001
T6f*	Recrystallized limestone	0.06	0.03	0.09	0.11	56.24	0.01	0.04	0.01	0.01	0.10	0.001
Recrystallized limestone at contact with the breccia												
T7-4*	Contact with the milled matrix breccia	0.14	0.03	0.09	0.15	55.91	0.01	0.04	0.01	0.01	0.09	0.001
T-3A	Contact with the main breccia pipe	0.35	0.03	0.54	0.3	54.37	0.01	0.04	0.01	0.03	0.92	0.001
Recrystallized limestone clast from the breccia												
T-2	Recrystallized limestone clast	0.23	0.08	0.31	0.34	55.18	0.01	0.04	0.01	0.01	0.27	0.001
Recrystallized limestone at contact with the mineralization												
T6e*	Recrystallized limestone at contact with skarn mineral assemblage	0.16	0.03	0.74	0.11	52.92	0.01	0.04	0.01	0.01	3.67	0.001
T9-5*	Recrystallized limestone at contact with hydrothermal mineral assemblage	0.08	0.03	0.16	0.23	55.75	0.01	0.04	0.01	0.01	0.47	0.001
Syn-ore carbonates												
T6a-1*	Syn-ore carbonates, Skarn mineral assemblage	0.04	0.03	13.69	4.54	35.03	0.01	0.04	0.01	0.01	5.72	0.001
T9-5 (4)-1*	Syn-ore carbonates, Hydrothermal mineral assemblage	0.09	0.03	9.45	5.79	34.14	0.01	0.04	0.01	0.01	10.32	0.001
Post-ore carbonates												
T6a-2*	Post-ore carbonates, Skarn mineral assemblage	0.04	0.03	0.85	0.23	53.66	0.01	0.04	0.01	0.01	2.46	0.001
T7-2*	Post-ore carbonates, Hydrothermal mineral assemblage	0.05	0.03	0.16	0.22	54.04	0.01	0.04	0.01	0.01	2.88	0.001
T8a*	Post-ore carbonates, Hydrothermal mineral assemblage	0.04	0.03	0.74	0.25	53.29	0.01	0.04	0.01	0.01	3.19	0.001
T9-5 (4)-2*	Post-ore carbonates, Hydrothermal mineral assemblage	0.10	0.03	0.36	0.30	54.54	0.01	0.04	0.01	0.01	2.77	0.001

		Mo	Cu	Pb	Zn	Ni	As	Cd	Sb	Bi	Ag	Hg
						%		ppm				
Barren recrystallized limestone												
STS-0*	Recrystallized limestone	<d.l.	0.9	5.1	7	1.3	0.9	0.2	0.1	<d.l.	<d.l.	<d.l.
KM10*	Recrystallized limestone	<d.l.	0.3	6.1	16	2.1	1.2	0.2	0.1	<d.l.	<d.l.	0.01
T6f*	Recrystallized limestone	0.1	0.3	6.8	6	1.7	<d.l.	0.1	0.2	<d.l.	<d.l.	0.02
Recrystallized limestone at contact with the breccia												
T7-4*	Contact with the milled matrix breccia	<d.l.	0.4	30.6	12	2.4	1.5	0.3	0.6	<d.l.	<d.l.	0.01
T-3A	Contact with the main breccia pipe	0.1	0.9	12.2	10	0.2	31.1	0.1	0.5	0.1	<d.l.	<d.l.
Recrystallized limestone clast from the breccia												
T-2	Recrystallized limestone clast	0.1	0.2	25.9	8	1.3	40.9	0.1	0.4	1.0	0.2	0.01
Recrystallized limestone at contact with the mineralization												
T6e*	Recrystallized limestone at contact with skarn mineral assemblage	0.3	0.2	6.7	3	1.0	2.2	<d.l.	0.1	<d.l.	<d.l.	<d.l.
T9-5*	Recrystallized limestone at contact with hydrothermal mineral assemblage	0.1	0.4	7.2	10	3.4	<d.l.	0.2	0.3	<d.l.	<d.l.	0.01
Syn-ore carbonates												
T6a-1*	Syn-ore carbonates, Skarn mineral assemblage	0.4	0.4	26.3	49	0.1	62.9	0.3	1.3	0.1	<d.l.	0.01
T9-5 (4)-1*	Syn-ore carbonates, Hydrothermal mineral assemblage	0.9	79.5	399.9	238	<d.l.	727.0	1.6	7.9	0.1	0.8	0.01
Post-ore carbonates												
T6a-2*	Post-ore carbonates, Skarn mineral assemblage	0.2	0.1	15.0	11	0.4	6.2	0.1	0.5	0.1	<d.l.	0.02
T7-2*	Post-ore carbonates, Hydrothermal mineral assemblage	0.3	1.9	600.5	111	1.2	14.8	0.9	2.1	<d.l.	1.1	<d.l.
T8a*	Post-ore carbonates, Hydrothermal mineral assemblage	0.3	0.2	8.8	26	0.4	6.3	0.2	0.9	<d.l.	<d.l.	<d.l.
T9-5 (4)-2*	Post-ore carbonates, Hydrothermal mineral assemblage	0.2	0.2	53.3	60	0.1	1.2	0.5	0.2	<d.l.	<d.l.	0.01

<d.l. - below detection llimit
* - major element and REE content adopted from STRMIĆ PALINKAŠ et al. (2013)

Table 2. Chemical composition of carbonates from the Trepča Pb-Zn-Ag skarn deposit.

		Ba	Cs	Ga	Rb	Sr	Th	U	W	Zr	Y	La
						%		ppm				
Barren recrystallized limestone												
STS-0*	Recrystallized limestone	7.0	<d.l.	<d.l.	0.7	243	0.2	<d.l.	<d.l.	1.6	2.6	1.3
KM10*	Recrystallized limestone	3.3	<d.l.	0.8	0.6	153.1	<d.l.	<d.l.	<d.l.	0.7	0.8	0.8
T6f*	Recrystallized limestone	6.0	<d.l.	1.7	0	210	<d.l.	0.3	<d.l.	0.8	0.8	0.8
Recrystallized limestone at contact with the breccia												
T7-4*	Contact with the milled matrix breccia	2.3	<d.l.	0.6	0.7	332.4	<d.l.	0.2	<d.l.	0.5	0.6	<d.l.
T-3A	Contact with the main breccia pipe	4.7	<d.l.	<d.l.	1.3	164.4	<d.l.	0.1	0.2	1.0	4.1	2.1
Recrystallized limestone clast from the breccia												
T-2	Recrystallized limestone clast	7.4	<d.l.	<d.l.	0.8	200.8	<d.l.	<d.l.	0.3	1.3	1.2	0.9
Recrystallized limestone at contact with the mineralization												
T6e*	Recrystallized limestone at contact with skarn mineral assemblage	5.1	0.3	2.6	<d.l.	64.1	<d.l.	<d.l.	<d.l.	<d.l.	36.9	28.6
T9-5*	Recrystallized limestone at contact with hydrothermal mineral assemblage	6.1	0.1	<d.l.	0.8	108.2	<d.l.	0.2	<d.l.	1.2	3.0	1.4
Syn-ore carbonates												
T6a-1*	Syn-ore carbonates, Skarn mineral assemblage	3.9	0.5	1.6	<d.l.	104	<d.l.	0.1	0.9	<d.l.	27.4	17.0
T9-5 (4)-1*	Syn-ore carbonates, Hydrothermal mineral assemblage	14.1	0.1	1.2	<d.l.	120.1	<d.l.	<d.l.	0.2	<d.l.	9.5	4.4
Post-ore carbonates												
T6a-2*	Post-ore carbonates, Skarn mineral assemblage	9.4	<d.l.	<d.l.	<d.l.	328.3	0	0.8	<d.l.	<d.l.	4.5	0.9
T7-2*	Post-ore carbonates, Hydrothermal mineral assemblage	5.2	<d.l.	<d.l.	<d.l.	229.7	0	0.2	0.2	<d.l.	2.9	0.8
T8a*	Post-ore carbonates, Hydrothermal mineral assemblage	4.3	<d.l.	0.6	<d.l.	181.2	0	0.5	<d.l.	0.5	5.7	2.1
T9-5 (4)-2*	Post-ore carbonates, Hydrothermal mineral assemblage	2.9	<d.l.	1.2	<d.l.	316.3	0	0.3	<d.l.	<d.l.	8.3	2.1

		Ce	Pr	Nd	Sm	Eu	Gd	Tb	Dy	Ho	Er	Tm
						%		ppm				
Barren recrystallized limestone												
STS-0*	Recrystallized limestone	1.2	0.24	0.9	0.2	<d.l.	0.39	0.05	0.18	0.05	0.16	<d.l.
KM10*	Recrystallized limestone	0.6	0.08	<d.l.	<d.l.	<d.l.	0.07	0.01	0.06	<d.l.	<d.l.	<d.l.
T6f*	Recrystallized limestone	<d.l.	0.06	<d.l.	<d.l.	<d.l.	0.06	0.02	0.05	<d.l.	0.05	<d.l.
Recrystallized limestone at contact with the breccia												
T7-4*	Contact with the milled matrix breccia	<d.l.	0.05	<d.l.	<d.l.	<d.l.	<d.l.	<d.l.	0.06	<d.l.	<d.l.	<d.l.
T-3A	Contact with the main breccia pipe	4.2	0.51	2.1	0.5	0.48	0.63	0.10	0.51	0.10	0.32	<d.l.
Recrystallized limestone clast from the breccia												
T-2	Recrystallized limestone clast	0.9	0.12	0.6	<d.l.	0.08	0.10	0.01	0.08	<d.l.	0.09	<d.l.
Recrystallized limestone at contact with the mineralization												
T6e*	Recrystallized limestone at contact with skarn mineral assemblage	67.7	8.41	37.0	8.9	6.50	8.67	1.24	7.13	1.19	3.00	0.35
T9-5*	Recrystallized limestone at contact with hydrothermal mineral assemblage	0.5	0.23	0.9	0.2	0.14	0.25	0.05	0.26	0.08	0.20	<d.l.
Syn-ore carbonates												
T6a-1*	Syn-ore carbonates, Skarn mineral assemblage	26.4	2.92	11.2	3.0	6.46	3.52	0.68	4.36	0.84	2.48	0.31
T9-5 (4)-1*	Syn-ore carbonates, Hydrothermal mineral assemblage	7.6	0.92	3.8	1.3	3.35	1.70	0.24	1.41	0.24	0.59	0.08
Post-ore carbonates												
T6a-2*	Post-ore carbonates, Skarn mineral assemblage	1.7	0.20	1.4	0.3	0.52	0.54	0.08	0.50	0.11	0.41	0.05
T7-2*	Post-ore carbonates, Hydrothermal mineral assemblage	1.2	0.13	0.8	0.1	0.26	0.39	0.05	0.35	0.08	0.21	<d.l.
T8a*	Post-ore carbonates, Hydrothermal mineral assemblage	3.1	0.42	1.8	0.4	0.50	0.88	0.11	0.66	0.14	0.38	0.06
T9-5 (4)-2*	Post-ore carbonates, Hydrothermal mineral assemblage	3.2	0.46	1.9	0.6	1.25	1.07	0.18	1.03	0.24	0.66	0.08

<d.l. - below detection llimit
* - major element and REE content adopted from STRMIĆ PALINKAŠ et al. (2013)

Table 2. Chemical composition of carbonates from the Trepča Pb-Zn-Ag skarn deposit.

		Yb	Lu	Sum REE	Au
			%	ppm	ppb
Barren recrystallized limestone					
STS-0*	Recrystallized limestone	0.13	0.03	4.83	0.5
KM10*	Recrystallized limestone	<d.l.	<d.l.	1.62	<d.l.
T6f*	Recrystallized limestone	0.05	0.01	1.1	0.5
Recrystallized limestone at contact with the breccia					
T7-4*	Contact with the milled matrix breccia	<d.l.	<d.l.	0.11	<d.l.
T-3A	Contact with the main breccia pipe	0.25	0.03	11.83	<d.l.
Recrystallized limestone clast from the breccia					
T-2	Recrystallized limestone clast	0.11	<d.l.	2.99	1.0
Recrystallized limestone at contact with the mineralization					
T6e*	Recrystallized limestone at contact with skarn mineral assemblage	1.69	0.25	180.63	1.1
T9-5*	Recrystallized limestone at contact with hydrothermal mineral assemblage	0.13	0.03	4.37	<d.l.
Syn-ore carbonates					
T6a-1*	Syn-ore carbonates, Skarn mineral assemblage	2.03	0.23	81.43	3.9
T9-5 (4)-1*	Syn-ore carbonates, Hydrothermal mineral assemblage	0.51	0.06	26.2	16.6
Post-ore carbonates					
T6a-2*	Post-ore carbonates, Skarn mineral assemblage	0.28	0.03	7.02	1.1
T7-2*	Post-ore carbonates, Hydrothermal mineral assemblage	0.15	0.03	4.55	<d.l.
T8a*	Post-ore carbonates, Hydrothermal mineral assemblage	0.30	0.05	10.9	<d.l.
T9-5 (4)-2*	Post-ore carbonates, Hydrothermal mineral assemblage	0.53	0.08	13.38	1.1

<d.l. - below detection llimit
* - major element and REE content adopted from STRMIĆ PALINKAŠ et al. (2013)

plied based on the relationships between the intensity of the first sample peak (m/z = 44) and $\delta^{18}O$ values of the standards. Due to calibration based directly on the Carrara marble standard, which were part of each run, correction for calcite runs was unnecessary. The stable carbon and oxygen isotope ratios are reported in the delta (d) notation as per mil (‰) deviation relative to the Vienna Standard Mean Ocean Water (V-SMOW) for oxygen and Vienna Pee Dee Belemnite (V-PDB) for carbon. The analytical precision was better than ±0.05‰ for $\delta^{13}C$ and ±0.1‰ for $\delta^{18}O$.

K/Ar dating was undertaken at the Institute of Nuclear Research of the Hungarian Academy of Science (ATOMKI), Debrecen. The whole rock samples were crushed to 0.063-0.315 mm size. Sanidine phenocrysts were hand-picked. One aliquot of samples (100 mg) was pulverized for potassium determination. Powders were digested in HF with the addition of some sulfuric and perchloric acids. The digested samples were dissolved in 100 ml 0.25 mol/1 HCl and diluted fivefold. Na and Li (100 ppm) were added as buffer and internal standard. The potassium concentration was measured with a digitalized flame photometer. Another aliquot of samples (500 mg) was used for Ar analyses. The samples were degassed by high-frequency induction heating, and the conventional getter materials were used for cleaning Ar. The ^{38}Ar spike was introduced to the system from a gas pipette before degassing. The cleaned Ar was directly introduced into the mass spectrometer, operated in the static mode. Recording and evolution of Ar spectra was controlled by a microcomputer. Details of the instruments, the applied methods and results of calibration have been described by BALOGH (1985).

4 RESULTS

4.1. GEOCHEMISTRY OF CARBONATES

The major element and REE contents of carbonates from the Trepča deposit are given in STRMIĆ PALINKAŠ et al. (2013). In this publication we refer to those data and present new unpublished trace element data obtained on the same set of samples (Table 2). In addition, the recrystallized limestone from the contact with the breccia pipe and a fragment of recrystallized limestone hosted by the breccia has been analyzed (Table 2).

The barren recrystallized Upper Triassic limestone (samples STS-0, KM10 and T6f) is characterized by a high CaO content (~56 wt. %) and a low content of aluminosilicate impurities (SiO_2< 0.22 wt. %, Al_2O_3< 0.07 wt. %). Large-ion-lithophile elements display low concentrations with an expected exception of Sr (210-332 ppm). The REE concentrations are mostly below their detection limits, precluding estimation of complete REE patterns for this group of carbonates.

The recrystallized limestone in contact with the breccia pipe (T3a) shows an increase in MnO (0.9 wt. %), Fe_2O_3 (0.5 wt. %), SiO_2 (0.35 wt. %), As (31.1 ppm), Pb (12.2 ppm), Y (4.1 ppm), Sb (0.5 ppm), W (0.2 ppm) and REE content (S_{REE} = 11.8 ppm). It exhibits the roof-shaped PAAS-normalized REE concentration pattern with a very negative Ce_N and a strong positive Eu_N anomaly (Fig. 6). The chemical composition of the recrystallized limestone in contact with the lateral branches of the main breccia pipe (T7-4) shows overlapping with the values obtained for the barren recrystallized limestone. However, some trace elements, including Pb (30.6 ppm), Ni (2.4 ppm), As (1.5 ppm), Cd (0.3 ppm), and Sb (0.6 ppm) are more abundant than in the barren limestone. Whereas the majority of REE have concentrations below their detection limits, the REE pattern cannot be plotted. The fragments of recrystallized limestone hosted by the breccia (T2) are slightly enriched in MnO (0.3 wt. %), Fe_2O_3 (0.3 wt. %), Pb (25.9 ppm), As (40.9 ppm), Sb (0.4 ppm), Ag (0.2 ppm), Au (1 ppb), Tl (0.1 ppm), and W content (0.3 ppm) comparing to the barren recrystallized Upper Triassic limestone. The complete REE pattern cannot be estimated due to concentrations of Sm, Dy, Tm and Lu below their detection limits, the ob-

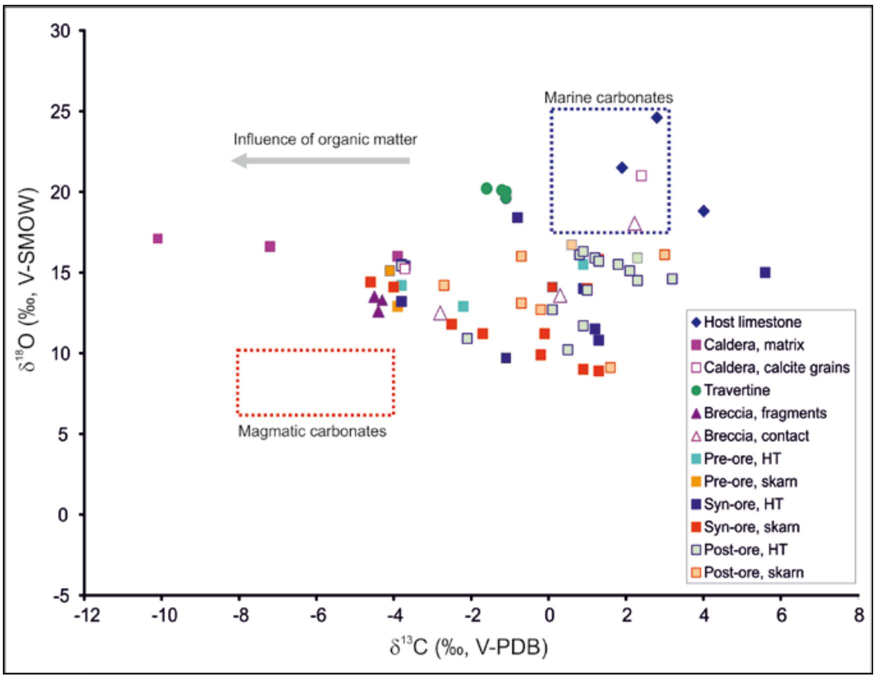

Figure 7. δ13C vs. δ18O plot of various carbonates from the Trepča Pb-Zn-Ag skarn deposit.

tained data suggest an enrichment in LREE over HREE, a week negative $Ce_N$and a prominent positive Eu_N anomaly (Fig. 6). The recrystallized limestone in contact with the skarn mineralization (T6e) is enriched in MnO (3.7 wt. %), Fe_2O_3 (0.7 wt. %), Y (36.9 ppm), REE (S_{REE} = 180.6 ppm), Au (1.1 ppb) and Mo (0.3 ppm). Concentrations of chalcophile elements are mostly within the same ranges as those obtained for the barren recrystallized limestone. Exceptions are As and Ga that show a slight increase. A decrease in Sr concentration positively correlates with a decrease in Ca content. The recrystallized limestone in contact with the hydrothermal mineralization (T9-6) is negligibly enriched in Mn and Fe comparedto the barren recrystallized Upper Triassic limestone (Table 2). Syn-ore carbonates (T6a-1, T9-5(4)-1) are significantly enriched in Fe (9.5-13.7 wt. % Fe_2O_3), Mg (4.5-5.8 wt. % MgO) and Mn (5.7-10.3 wt. % MnO). Large-ion-lithophile elements display low concentrations with the expected exception for Sr (104-120 ppm). Caesium is slightly increased in syn-ore carbonates associated with the skarn mineral assemblage. In contrast, syn-ore carbonates from the hydrothermal mineral assemblage are enriched in Ba (Table 2). Concentrations of high field strength elements are mostly below their detection limits, with an exception for Y and REE that are significantly increased compared to the barren recrystallized Upper Triassic limestone (Table 2). Syn-ore carbonates are enriched in chalcophile elements, including Ag (up to 0.8 ppm), As (62.9-727 ppm), Bi (0.1 ppm), Cd (0.3-1.6 ppm), Cu (0.4-79.5 ppm), Pb (26.3-400 ppm), Sb (1.3-7.9 ppm) and Zn (49-238 ppm), as well as in Au (3.9-16.6 ppb). Post-ore carbonates (T6a-2, T7-2, T8a, T9-5(4)-2) are depleted in Fe (0.2-0.9 wt. % Fe_2O_3), Mg (0.2-0.3 wt. % MgO), Mn (2.4-3.2 wt. % MnO) and the majority of chalcophile elements compared to syn-ore carbonates (Table 2). However, some post-ore carbonates may have increased concentrations of Pb (~600 ppm), Zn (~110 ppm) and Ag (~1 ppm).

4.2. STABLE ISOTOPE COMPOSITION OF CARBONATES

The $\delta^{18}O$ and $\delta^{13}C$ data obtained on the 68 carbonates from 34 hand specimens are listed in Table 3 and shown in Figure 7. The barren limestones have average $\delta^{13}C$ and $\delta^{18}O$ values of 2.9 ± 1.1 ‰ V-PDB and 21.9 ± 2.5 ‰ V-SMOW, respectively. The limestones in contact with the breccia together with the limestone fragments from the breccia are shifted toward significantly lower $\delta^{18}O$ values. Recrystallized limestones in contact with the skarn ($\delta^{13}C$ = -4.0 ± 0.1 ‰, $\delta^{18}O$ = 14.0 ± 1.5 ‰) and hydrothermal mineralization ($\delta^{13}C$ = 0.8 ± 2.8 ‰, $\delta^{18}O$ = 18.5 ± 4.2 ‰) differ in both their carbon and oxygen, isotopic composition. Syn-ore and post-ore carbonates exhibit depletion in ^{13}C and ^{18}O compared to the barren recrystallized limestone. Carbonates separated from the pyroclastic rocks of the caldera display variable $\delta^{13}C$ and $\delta^{18}O$ composition with values between -10 and -1 ‰ and 15.5 to -21 ‰, respectively. Travertine deposits have uniform isotopic composition with average $\delta^{13}C$ and $\delta^{18}O$ values of -1.2 ± 0.2 ‰ and 20.0 ± 0.3 ‰, respectively.

4.3. FLUID INCLUSION DATA

Fluid inclusions have been studied in transparent minerals, calcite and quartz, hosted by different types of breccia fragments and in the recrystallized limestone at its contacts with the breccia (Fig. 8). The data are summarized in Figure 9.

Calcite grains selected from the recrystallized limestone at the contact with the main breccia pipe (T3a, 75 m above mean sea level) host fluid inclusions of pseudosecondary and secondary origin. According to their petrographic features, three types of fluid inclusion assemblages have been distinguished: Type 1) Assemblages composed of two phase, L-rich inclusions (Fig. 8a); Type 2) Assemblages that contain coexisting L-rich and V-rich inclusions (Fig. 8b); and Type 3) Assemblages of two phase, V-rich inclusions (Fig. 8c). Liquid-rich

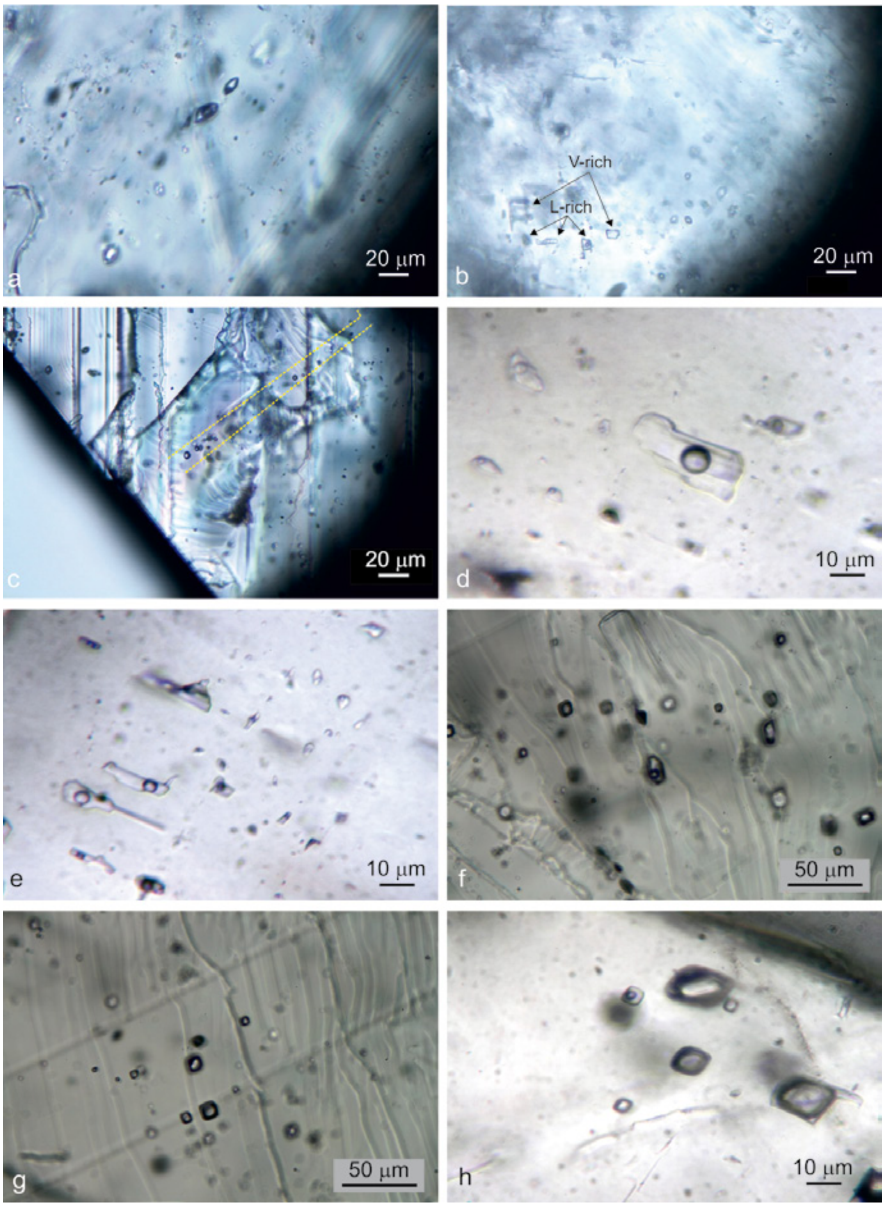

Figure 8. a. Pseudosecondary L-rich fluid inclusion assemblages from the recrystallized limestone at the contact with the main breccia pipe; b. Pseudosecondary coexisting L- and V-rich fluid inclusions from the recrystallized limestone at the contact with the main breccia pipe; c. Pseudosecondary V-rich fluid inclusion assemblages from the recrystallized limestone at the contact with the main breccia pipe; d. Pseudosecondary L-rich fluid inclusion assemblages from the recrystallized limestone at the contact with the lateral breccia branches; e. Pseudosecondary L-rich fluid inclusion assemblages from calcite grains in clasts composed of a magnetite core and a pyrite rim; f. Boiling effect within calcite grains separated from clasts composed of a magnetite core and a pyrite rim; g. Vapour-rich inclusions in calcite grains selected from pyroclastic deposits; h. Two-phase aqueous fluid inclusions in calcite grains selected from pyroclastic deposits.

fluid inclusion assemblages (Type 1) can be subdivided into two subtypes according to their microthermometric data. Subtype 1a comprises L-rich inclusions with the degree of fill around 0.7 and homogenization temperatures (T_h) between 343 and 370°C (Fig. 9). They have a eutectic temperature (T_e) near -50°C suggesting $CaCl_2$, NaCl and KCl as the principal salts dissolved in the aqueous solution (BORISENKO, 1977; SAMSON & WALKER, 2000). The salinity in the range between 19.8 to 20.6 wt.% NaCl equ. (Fig. 9) is estimated from the final ice melting temperature ($T_{m\ ice}$) recorded in the interval between -16.5 and -17.5°C (BODNAR, 1993). Subtype 1b comprises L-rich inclusions with the degree of fill around 0.8 and T_h recorded between 275 and 290°C (Fig. 9). Eutectic temperatureswere recorded around -50°C as well, but salinities in the range between 2.6 and 4.2 wt.% NaCl equ. ($T_{m\ ice}$ = -1.5 to -2.5°C) are significantly lower than the values obtained for the former subtype of L-rich inclusions (Fig. 9). Fluid inclusion assemblages comprising coexisting L-rich and V-rich inclusions (Type 2) suggest an entrapment of boiling fluids (BODNAR et al., 1985). Liquid-rich inclusions have a variable degree of fill, varying between 0.6 up to 0.8. The T_e near -50°C was recorded in several fluid inclusions revealing $CaCl_2$, NaCl and KCl as the principal dissolved salts. Whereas this type of fluid inclusion has a salinity greater than 23 wt. % NaCl equ., the ice dissolution precedes the hydrohalite dissolution. In some inclusions hydrohalite melts as the final solid phase. The final melting temperature in the interval between -3.2 and 0°C suggests salinities between 25.8 and 26.2 wt.% NaCl equ. (Fig. 9; STERNER et al., 1988). In other inclusions of this type, hydrohalite was transformed into halite at temperatures around 0°C. Halite dissolves at temperatures up to 7°C pointing to the maximum salinity of 26.3 wt.% NaCl equ. (STERENER et al., 1988). Total homogenization occurs by vapour phase disappearance in the temperature range between 285 and 305°C (Fig. 9). Phase transitions in V-rich inclusions have not been recorded. Fluid inclusion assemblages that contain only V-rich inclusions (Type 3) have been recorded as well but the ambiguous phase transitions preclude their interpretation.

The recrystallized limestone at the contact with lateral branches filled with the milled matrix fluidized breccia (T4, T7-4) hosts visible fluid inclusions only in calcite grains very close to the breccia-limestone contact. Already at 5 cm from the contact inclusions become too small for reliable measurements (<5 µm). At a distance of 10 cm from the contact fluid inclusions have not been detected. Measurable fluid inclusions are L-rich, with the degree of fill around 0.7 to 0.8 (Fig. 8d). Homogenization into the liquid phase was recorded in the temperature interval from 360 to 375°C (Fig. 9). Ice melting occurred between -7.4 and -9°C corresponding to the salinity of 11.0 to 12.9 wt.% NaCl equ. (Fig. 9).

The clasts that comprise a magnetite core and a pyrite rim (KM7-1, KM8) were sampled from the surface (835 m above

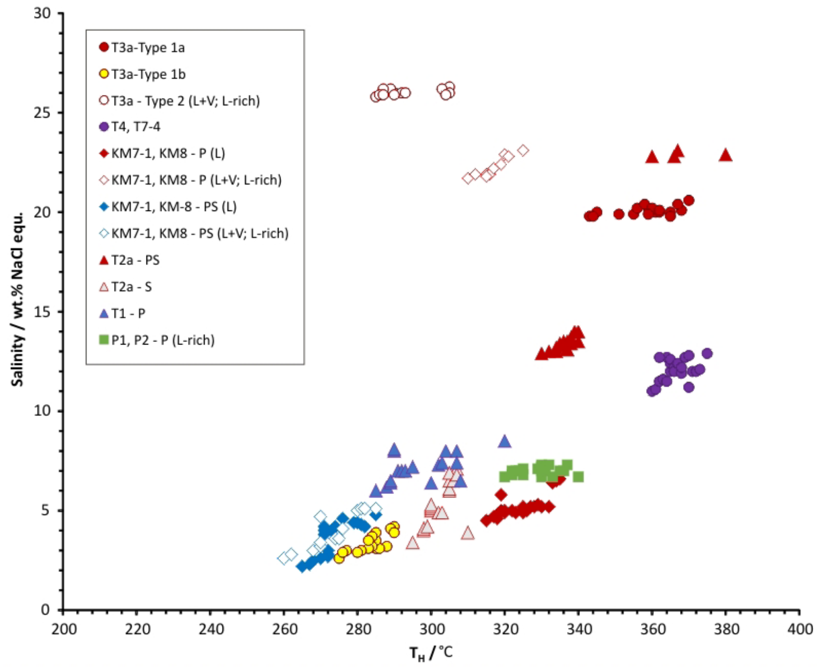

Figure 9. Correlation of homogenization temperature (TH) and salinity for fluid inclusions hosted at contacts of the phreatomagmatic breccia and its host rocks as well as within different types of clasts and pyroclastic rocks.

mean sea level). Over 80% of the primary and pseudosecondary fluid inclusions within calcite crystals belong to the two-phase, L-rich, type. They vary in size up to 25 mm (Fig. 8e). Primary fluid inclusion assemblages homogenized into the liquid phase in the interval between 315 and 335°C (Fig. 9). The first melting (near-eutectic) temperature around -52 ºC suggests that $CaCl_2$, NaCl and KCl are the principal dissolved salts (BORISENKO, 1977; SAMSON & WALKER, 2000). The $T_{m\ hyd}$ value recorded in the range between -27.7 and -29.1°C coincides with the NaCl/(NaCl+$CaCl_2$) mass ratio between 34 and 41 %. The $T_{m\ ice}$ in the range between -2.7 and -4.1°C corresponds to an apparent salinity of4.5 to 6.6 wt.% NaCl equ. (Fig. 9). Locally, the boiling effect is perceived. It is characterized by fluid inclusion assemblages comprising coexisting liquid- and vapour-rich fluid inclusions (Fig. 8f) with overlapping values of homogenization temperatures between 310 and 325°C (Fig. 9). Liquid-rich inclusions have relatively high salinities ($T_{m\ ice}$ = -19.1 to -21.0°C; salinity = 21.7 to 23.1 wt.% NaCl equ.; Fig. 9). Pseudosecondary fluid inclusion assemblages mostly comprise liquid-rich fluid inclusions with homogenization temperatures between 265 and 285°C (Fig. 9). Their apparent salinity ranges between 2.2 and 4.8 wt.% NaCl equ. (Fig. 9; $T_{m\ ice}$ = -1.3 to -2.9°C). In addition, several fluid inclusion assemblages composed of coexisting liquid- and vapour-rich inclusions have been recorded. Their homogenization temperatures mostly overlap with those obtained for the liquid-rich pseudosecondary fluid inclusion assemblages, but they have slightly greater salinities (Fig. 9; $T_{m\ ice}$ = -1.5 to -3.2°C; salinity = 2.6 to 5.1 wt.% NaCl equ.).

In the deeper part of the breccia, at horizon X (75 m above mean sea level), several different types of fragments were studied. Microthermometry on the majority of barren recrystallized limestone fragments (T2) was hampered, due to the presence of only monophase fluid inclusions. In contrast, recrystallized limestone fragments accompanied with fibroradial arsenopyrite and magnetite (T2a) have been eligible for microthermometric studies. Pseudosecondary fluid inclusion assemblages are overprinted by secondary fluids. Both fluid inclusion generations are characterized by T_e around -50°C ($CaCl_2$-NaCl±KCl-H_2O system). Pseudosecondary fluid inclusions show $T_{m\ hyd}$ in the range between -27.0 and -28.5°C indicating the NaCl/(NaCl+$CaCl_2$) mass ratio between 37 and 45 %. The majority of fluid inclusions have moderate salinities in the range between 12.9 and 14.0 wt.% NaCl equ. (Fig. 9; $T_{m\ ice}$ = -9.0 to -10.0°C) and homogenize into liquid phase in the temperature interval from 330 to 340°C (Fig. 9). Several inclusions with higher salinity ($T_{m\ ice}$ = -20.5 to -21.0°C; salinity = 22.8 to 23.1 wt.% NaCl equ.) have also been recorded (Fig. 9). Due todecrepitation before homogenization, usually between 320 and 340°C, only a few total homogenizations into the liquid phase were obtained in the range from 360 to 380°C (Fig. 9). Secondary inclusions have $T_{m\ hyd}$ in the interval from -22.1 to -26.0°C (the NaCl/(NaCl+$CaCl_2$)mass ratio = 52-89 %), $T_{m\ ice}$ between -2.0 and -4.5°C (salinity = 3.4-7.1 wt.% NaCl equ.) and T_H from 295 to 310°C (Fig. 9).

Quartz separated from the carbonate fragments within the main breccia (T1) was suitable for microthermometric investigations. Quartz is represented by euhedral crystals accompanied bydickite aggregates. Primary L-rich fluid inclusions homogenize to a liquid phase at temperature between 285 and 320°C (Fig. 9). Their salinities range from 6.0 to 8.5 wt.% NaCl equ. (Fig. 9). Secondary inclusions have not been observed probably due to their small size.

Table 3. Carbon and oxygen isotope composition of carbonates from the Trepča Pb-Zn-Ag skarn deposit.

Sample	**Level**	**Type of mineralization**	**Description**	**$\delta^{13}C$ (‰, V-PDB)**	**$\delta^{18}O$ (‰, V-SMOW)**
Barren limestone					
T6f	X	host limestone, barren, recrystallized	white recrystallized carbonate	1.9	21.5
KM-10	surface	host limestone, barren, recrystallized	greyish calcite crystals	2.8	24.6
STS-0	X	host limestone, barren, recrystallized	greyish recrystallized carbonate	4	19.6
Carbonate from pyroclastic rocks					
P1-1	surface	caldera	matrix, grey calcite	-10.1	17.1
P1-2	surface	caldera	white calcite grain	-3.7	15.6
P1-3	surface	caldera	matrix	-3.9	16
P2-1	surface	caldera	matrix	-7.2	16.6
P2-2	surface	caldera	white calcite grain	2.4	21
Travertine deposit					
P4-1	surface	travertine deposit	grayish to dark purple travertine	-1.1	19.6
P4-2	surface	travertine deposit	grayish to dark purple travertine	-1.1	20
P4-3	surface	travertine deposit	grayish to dark purple travertine	-1.2	20.1
P4-4	surface	travertine deposit	grayish to dark purple travertine	-1.6	20.2
Carbonate from breccia					
T2-1	X	recrystallized limestone fragment	grey massive carbonate	-4.3	13.3
T2-2	X	recrystallized limestone fragment	white massive carbonate	-4.4	12.6
T2a-1	X	recrystallized limestone fragment with magnetite and arsenopyrite	white calcite grain (rhombohedral)	-4.5	13.5
Carbonate at contact with breccia					
T3-1	X	late phase calcite	white calcite crystals (elongated, scalenohedral)	0.4	13.5
T3-2	X	recrystallized limestone, barren	white massive carbonate	-2.8	12.5
T7-4-1	X	recrystallized limestone, barren	greyish calcite crystals	2.2	17.9
Hydrothermal parageneses, pre-ore					
TR-VII-7	VII	recrystallized carbonate	grey calcite crystals	2.9	22.8
TR-XI-2-1	XI	recrystallized carbonate	grey calcite crystals	2.8	22.2
TR-XI-2-2	XI	recrystallized carbonate	yellowish calcite crystals	-3.8	14.2
TR-XI-5-1	XI	recrystallized carbonate	yellowish calcite crystals	0.9	15.5
TR-XI-6-1	XI	recrystallized carbonate	white calcite grain (rhombohedral)	-2.2	12.9
TR-XI-3-1	XI	recrystallized carbonate	grey calcite crystals	3	21
T9-5-A-1	X	recrystallized carbonate	grey calcite grain	2.3	20.9
Skarn parageneses, pre-ore					
T6e	X	crystallized carbonate	white calcite crystals	-4.1	15.1
T9-6-1	X	massive carbonate	yellow-pinkish massive carbonate	-3.9	12.9
Hydrothermal parageneses, syn-ore					
TR-VIII-2-1	VIII	carbonate impregnated with galena	white massive carbonate	-1.1	9.7
TR-VIII-4-1	VIII	carbonate impregnated with galena	yellow massive carbonate	-3.8	15.5
TR-XI-4-2	XI	carbonate co-existing with quartz	white calcite grain	1.2	11.5
STS-1	X	massive carbonate with mineralization	yellow-pinkish massive carbonate (light)	-3.7	15.4
STS-3	X	massive carbonate	grey massive carbonate	-0.8	18.4
T7-2-2	X	calcite cogenetic with sph mineralization	white calcite veins	5.6	15
148A-1	X	calcite cogenetic with py mineralization	white calcite veins	0.9	14
T8-2-2	IX	calcite cogenetic with sph mineralization	white calcite veins	1.3	10.8
T9-5-4	X	carbonate impregnated with sph and py	white massive carbonate	-3.8	13.2

Table 3. Continuated

Sample	Level	Type of mineralization	Description	δ^{13}C (‰, V-PDB)	δ^{18}O (‰, V-SMOW)
Skarn parageneses, syn-ore					
T6-W	X	white carbonate associated with quartz alteration of hedenbergite	white carbonate, fine-grained	0.1	14.1
T6-Y	X	yellow carbonate associated with quartz alteration of hedenbergite	yellow carbonate, fine-grained	1.3	15.8
T6-G	X	grey carbonate associated with quartz alteration of hedenbergite	grey carbonate, fine-grained	-2.5	11.8
T6a-1	X	1st carbonate after sph mineralization	pink	-4.6	14.4
T6a-2	X	2nd carbonate after sph mineralization	yellow massive carbonate	-0.1	11.2
T6a-3	X	3rd carbonate after sph mineralization	white massive carbonate	1	14
T6b-1	X	1st carbonate after sph mineralization	pink	-4	14.1
T6b-2	X	2nd carbonate after sph mineralization	yellow massive carbonate	-0.2	9.9
T9-1-2	X	carbonate in conntact with quartz	yellow massive carbonate	0.9	9
T9-3-1	X	carbonate in conntact with quartz	white massive carbonate	1.3	8.9
T9-4-2	X	carbonate cogenetic with py mineralization	yellow massive carbonate	-1.7	11.2
Hydrothermal parageneses, post-ore					
TR-V-1	V	last phase calcite	grey calcite crystals (elongated, scalenohedral)	2.3	15.9
TR-VIII-2-2	VIII	last phase calcite	white calcite crystals (elongated, scalenohedral)	0.9	11.7
TR-VIII-4-2	VIII	last phase calcite	white calcite crystals (elongated, scalenohedral)	0.1	12.7
STS-2	X	massive carbonate, late phase	yellow-pinkish massive carbonate (dark)	-3.8	15.4
T5-1	X	last phase calcite	white calcite crystals (rhombohedral, vertical)	1.8	15.5
T7-2-1	X	last phase calcite	white calcite crystals (rhombohedral, vertical)	3.2	14.6
T7-2-3	X	last phase calcite	white calcite crystals (rhombohedral, vertical)	2.3	14.5
T7-3a-1	X	last phase calcite	white calcite crystals (rhombohedral)	2.1	15.1
T7-5-1	X	last phase calcite	white calcite crystals (rhombohedral)	0.8	16.1
T8a-1	IX	last phase calcite	white calcite crystals (rhombohedral)	1.2	15.9
T8-2-1	IX	last phase calcite	white calcite crystals (rhombohedral)	0.9	16.3
T9-5-1	X	last phase calcite (5mm to sph min)	white calcite crystals (rhombohedral)	0, 5	10.2
T9-5-2	X	last phase calcite (10mm to sph min)	white calcite crystals (rhombohedral)	1	13.9
T9-5-A-4	X	last phase calcite	white calcite crystals (rhombohedral)	1.3	15.7
T9-5-A-5	X	phase before the last	white calcite crystals (rhombohedral)	-2.1	10.9
Skarn parageneses, post-ore					
T6-1	X	last phase calcite	white calcite crystals (rhombohedral)	0.6	16.7
T9-1-1	X	last phase calcite	white calcite crystals (rhombohedral, vertical)	-0.7	13.1
T9-4-1	X	last phase calcite	white calcite crystals (rhombohedral, isometric)	3	16.1
T9-4-3	X	last phase calcite	white calcite crystals (rhombohedral, isometric)	-0.2	12.7
T9-6-2	X	last phase calcite	white calcite crystals (rhombohedral)	-0.7	16
T9-6-(4)-1	X	last phase calcite	white calcite crystals (rhombohedral, vertical)	-2.7	14.2
T9-6-(4)-2	X	phase before the last	white calcite crystals (rhombohedral)	1.6	9.1

Two types of fluid inclusions were recognized in calcite grains hosted by pyroclastic material of the caldera (P1, P2): 1) Vapour-rich inclusions represent the majority of the inclusion population (Fig. 8g). This type of FIs are resistant to developing phases during extreme cooling to the temperature of liquid nitrogen and heating up to 400°C, and 2) Two-phase aqueous fluid inclusions consist of vapour and liquid water at room temperature (Fig. 8h). Two-phase inclusions can be subdivided into liquid-rich and vapour-rich subtypes according to their vapour to liquid ratio. Coexistence of inclusions with miscellaneous degrees of filling suggests inhomogeneous trapping from boiling fluid (Fig. 7). The near-eutectic temperature observed within liquid-rich inclusions around -50°C reflects the $CaCl_2$-NaCl-±KCl-H_2O compositional model. $T_{m\ ice}$ in the range between -4.2 and -4.6°C corresponds to a salinity of between 6.7 and 7.3 wt.% NaCl equ. (Fig. 9). Homogenizations recorded in the same temperature interval for liquid-rich and vapour-rich inclusions (320-340°C; Fig. 9) suggest formation under boiling conditions.

4.4. K/Ar DATA

K-Ar ages obtained on samples from the phreatomagmatic breccia at the Trepča Pb-Zn-Ag skarn deposit are reported in Table 4. Sanidine and whole rock analysis of hydrothermally altered quartz-latite gave two almost concordant ages of 24.0 ± 0.7 and 25.1 ± 0.9 Ma, respectively. Dating of the milled breccia reveals ages of 20.9 ± 1.7 and 23.2 ± 0.7 Ma. The younger age is unreliable due to a low amount of radiogenic Ar and a large uncertainty.

5. DISCUSSION

This paper focuses on the breccia pipe and its role in ore-forming processes at the Trepča Pb-Zn-Ag skarn deposit. The P-T-X conditions during breccia emplacement were estimated from descriptive features, mineralogy, stable isotope and fluid inclusion data obtained from the breccia fragments and wall rocks.

The Trepča deposit was formed during three distinctive stages that are common for all types of skarn deposits elsewhere: (1) the stage of isochemical contact metamorphism during igneous rock emplacement, (2) the prograde stage characterized by metasomatic replacement of carbonate rocks with anhydrous silicate minerals, and (3) the retrograde hydrous stage that resulted in the alteration of earlier-formed mineral assemblages. Deposition of ore minerals accompanies stages 2 and 3 (e.g. MEINERT et al., 2005).

5.1. THE STAGE OF ISOCHEMICAL CONTACT METAMORPHISM

The isochemical contact metamorphism stage resulted in recrystallization of the country rocks (Upper Triassic limestone and schist, Fig. 2). The size of calcite grains in the recrystallized limestone varies from several millimetres, at places spatially distal to the mineralization and the breccia pipe, up to several centimetres near the contact with the ore bodies and the breccia. The absence of fluid inclusions from the barren recrystallization limestone suggests recrystallization without involvement of either H_2O or CO_2. The barren recrystallized limestone is characterized by a high CaO content and REE patterns with the negative Ce_N anomaly that are typical for marine carbonates (ELDERFIELD & GREAVES, 1982; HU et al., 1988). Furthermore, the average $\delta^{13}C$ value of the barren recrystallized limestone corresponds well to the worldwide Phanerozoic marine carbonate values (VEIZER & HOEFS, 1976) and $\delta^{18}O$ values are consistent with the Triassic marine carbonate values (CLAYPOOL et al., 1980). Obviously, the chemical and isotope composition of the limestone were not significantly disturbed by the recrystallization processes.

5.2. THE PROGRADE ANHYDROUS STAGE

The host recrystallized limestone at the contact with the prograde (skarn) mineralization is depleted in ^{13}C and ^{18}O, reflecting the contribution of magmatic CO_2 (ZHENG & HOEFS, 1993; ROSATELLI et al., 2010). The increased content of Fe, Mn, Mo, As, Au, Cs, Ga, REE and Y suggests that the listed elements were transported by infiltrating magmatic fluids.

5.3. THE MAIN BRECCIA - LIMESTONE CONTACT

Fluid inclusions are abundant in calcite crystals of the recrystallized limestone near contacts with the main breccia pipe and its lateral branches suggesting that aqueous fluids, channeled by the breccia, were involved in the recrystallization processes. Multiple generations of fluid inclusions that have been found at the contact with the main breccia pipe give an insight into the P-T-X characteristics of fluids involved in breccia formation processes. The high-temperature (T_H=343-370°C) and high salinity (19.8-20.6 wt.% NaCl equ.) L-rich fluid inclusion assemblages (Subtype 1a, Fig. 8a) represent the earliest among all recorded fluid inclusion generations. To keep fluids in the liquid phase at temperatures above 343°C the pressure should exceed 18 MPa (Fig. 10). The high pressure possibly reflects lithostatic conditions that preceded breccia formation. The travertine deposits found at the Trepča deposit surface (approximately 850 m above mean sea level) mark the preserved palaeosurface and allow estimation of the palaeodepth. The analyzed recrystallized limestone-breccia contact (sample T3a, 75 m above mean sea level) occurs around 775 m below the palaeosurface implying the lithostatic pressure of 21 MPa. The pressure correction applied to the representative isochores (Fig. 10) suggests the formation temperature between 350 and 370°C. The fluid inclusion assemblages that comprise coexisting L-rich and V-rich inclusions (Type 2, Fig. 8b) reflect boiling conditions probably related to decompression of the system from a lithostatic to hydrostatic regime due to the brecciation (STRMIĆ PALINKAŠ et al., 2014). Assuming the fluid salinity around 20 wt. % NaCl, the homogenization temperature between 285 and 305°C corresponds to adepth between 600 and 800 m below the former water table (Fig. 11). Boiling resulted in the separation of high salinity L-rich and low salinity V-rich inclusions. The fluid temperature drop from 350-370°C to 285-305°C suggests an adiabatic process and allows the calculation of the steam loss (e.g., SIMPSON et al., 2015):

$$H_{L,Tf(\text{Subtype 1a})} = (1-y)\times H_{L,Th(\text{L-rich, Type 2})} + y\times H_{V,Th(\text{L-rich, Type 2})} \qquad (1)$$

In this equation, $H_{L,Tf(\text{Subtype 1a})}$ represents an average specific enthalpy of the fluid before boiling at the temperature estimated from the pressure corrected representative isochores for Subtype 1a fluid inclusions (Fig. 10), $H_{L,Th(\text{L-rich, Type 2})}$ and $H_{V,Th(\text{L-rich, Type 2})}$ are average specific enthalpies of liquid and vapor phases separated during boiling at temperature equal to the homogenization temperature of L-rich inclusions coexisting with V-rich inclusions, and y is the steam (vapour) fraction. The specific enthalpies for liquid and vapour phases (assuming pure H_2O) were adopted from KEENAN et al. (1969). The calculated steam loss ranges around 30%. The fluid inclusion assemblages composed

Table 4. The K/Ar data obtained at the Trepča Pb-Zn-Ag skarn deposit.

Sample	Sample description	Dated fraction	K %	^{40}Ar* cm^3/g	^{40}Ar* %	K/Ar age (Ma)
TR-6	Surface, hydrothermaly altered quartz-latite	Sanidine	8.54	8.035×10-6	86.7	24.0 ± 0.7
		Whole rock	2.77	2.787×10-6	55.1	25.1 ± 0.9
T7-4a	Level X., milled breccia	Whole rock	2.43	1.985×10-6	16.7	20.9 ± 1.7
T4a	Level X., milled breccia	Whole rock	8.01	7.277×10-6	82.7	23.2 ± 0.7

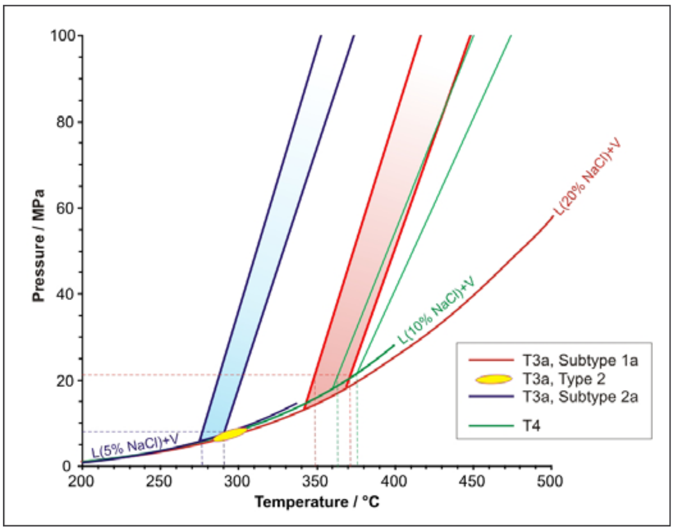

Figure 10. Pressure-temperature diagram showing the ranges of isochores for L-rich fluid inclusions hosted within the recrystallized limestone at its contact with the main breccia pipe (sample T3a, 75 m above mean sea level) and its contact with the lateral breccia branches (sample T4, 75 m above mean sea level). The boiling conditions obtained from the fluid inclusion assemblage composed of coexisting L-rich and V-rich inclusions are plotted too (Type 2, sample T3a, 75 m above mean sea level). The liquid-vapour curve for H_2O-NaCl fluids with 5, 10 and 20 wt % NaCl is adopted from BODNAR & VITYK (1994).

only of V-rich inclusions (Type 3) reveal that fluids periodically were completely converted to vapour, probably due to episodic fluxes of hot magmatic fluids. Assuming the palaeodepth of around 775 m, the pressure correction applied to the representative isochores for the moderate-temperature (T_H=275-290°C) and low salinity (2.6-4.2 wt.% NaCl equ.) L-rich fluid inclusion assemblages (Subtype 1b, Fig. X1) reveals their entrapment temperature between 275 and 290°C. Cooling and dilution of the fluids may reflect a contribution of descending groundwaters in the later stages of breccia formation.

The recrystallized limestone at the contact with the main breccia pipe (T3a) shows an increase in SiO_2, Fe_2O_3, and MnO content accompanied with the depletion in the CaO content comparing to the composition of the barren recrystallized limestone placed distally from the breccia. Some trace elements, including Pb, As, Sb, W, Y and REE are also enriched. The REE pattern possesses a weak negative Ce_N anomaly and a prominent positive Eu_Nanomaly. Furthermore, the recrystallized limestone at the contact with the breccia is depleted in ^{13}C and ^{18}O indicating the contribution of isotopically light CO_2 (Fig. 7) probably of a magmatic origin (ZHENG & HOEFS, 1993; ROSATELLI et al., 2010).

5.4. LATERAL BRECCIA BRANCHES - LIMESTONE CONTACT

The lateral dyke-like branches infilled with the milled matrix represent non-venting branches of the main phreatomagmatic breccia (CORBETT & LEACH, 1998). The hydraulic fracturing of country rocks requires a fluid pressure equal to the minimum principal stress plus the tensile strength of the rocks (JAEGER & COOK, 1979). The L-rich fluid inclusions found in the recrystallized limestone at contacts with the fissures indicate that recrystallization processes occurred in the presence of moderate salinity single phase (liquid) fluids that were channeled through the fissures. The minimum entrapment pressure was around 20 MPa (Fig. 10) suggesting that the pressure was controlled by lithostatic conditions. The pressure correction applied to the representative isochores, assuming the lithostatic conditions (Fig. 10), suggests the entrapment temperature was between 365 and 375°C. The abundant rock flour that was injected into such a type of fissures reflects transport by fluidization (McCALLUM, 1985; BRANQUET et al., 1999; CLARK & JAMES, 2003). The various types of hydrothermal alterations, including sericitization, kaolinitization, pyritization and carbonatization, that affected the rock flour suggest an intensive hydrothermal circulation. The major element composition and the REE content of the recrystallized limestone at this type of contacts (samples T4 and T7-4, 75 m above mean sea level) overlap with the values obtained for the barren recrystallized limestone placed distally from the breccia. However, some trace elements, including Pb, Ni, As, Cd and Sb are more abundant than in the barren limestone suggesting their transport by aqueous fluids. The δ^{13}C values overlap with values recorded for the barren recrystallized limestone revealing the negligible contribution of magmatic CO_2. In contrast, the decreased δ^{18}O values may be attributed to the involvement of aqueous fluids. According to the fractionation equation for a calcite-water pair (ZHANG, 1999), the fluid in the isotopic equilibrium with the analyzed calcite (δ^{18}O=17.9‰) at temperatures around 370°C should have and ^{18}O value of +13.7‰.

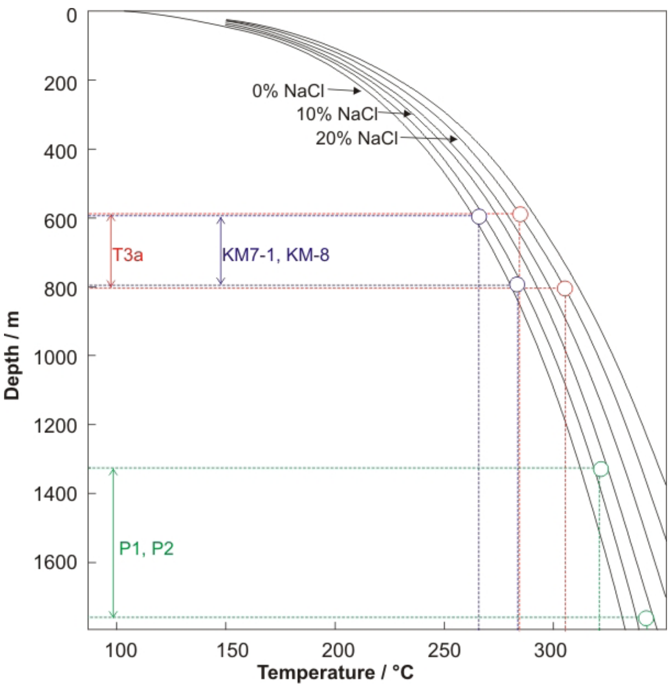

Figure 11. Fluid inclusion homogenization temperatures for coexistent liquid-rich and vapour-rich inclusions fitted on the boiling point-depth curves for fluids of different salinities (after HAAS, 1971) estimate the formation depths assuming the hydrostatic regime.

5.5. THE MAIN BRECCIA CLASTS

The clasts of country rocks and skarn mineralization that preceded the breccia formation underwent intense milling, mixing and hydrothermal alterations depending on their lithological characteristics and spatial position within the breccia. They show mutual differences in shape, dimension, composition, alteration, direction and distance of transport typical for phreatomagmatic breccias (e.g. SILLITOE, 1985; BAKER et al., 1986; TAMAS & MILESI, 2002). Sericitization of the breccia matrix, locally accompanied by minor kaolinitization, indicate increased water activity under near-neutral to weakly acidic conditions.

The fragments composed of a magnetite core and a pyrite rim (samples KM7-1, KM8; 835 m above mean sea level) suggest an increase in oxygen and sulfur fugacities over time (Fig. 12). Textural features suggest that the fibroradial magnetite core, accompanied by a mixture of quartz and carbonates, was formed by retrograde alteration of hedenbergite under increased oxygen fugacity:

$$3\ \mathrm{CaFe^{2+}Si_2O_6} + 3\ \mathrm{CO_2} + \tfrac{1}{2}\ \mathrm{O_2} \rightarrow \mathrm{Fe^{2+}Fe^{3+}{}_2O_4} + 3\ \mathrm{CaCO_3} + 6\ \mathrm{SiO_2} \quad (2)$$

hedenbergite *magnetite* *calcite* *quartz*

The fO_2 vs. fS_2 diagram constructed for the pre-breccia stage (lithostatic regime; $P \approx 20$ MPa; $T \approx 400$°C) and the main stage of the breccia formation (hydrostatic regime; $P \approx 7.5$ MPa; $T \approx 300$°C) reveals that hedenbergite stability strongly depends on temperature and pressure, favouring the prograde stage conditions (Fig. 12). The increased water activity and oxygen fugacity as well as the decreased temperature are direct consequences of the breccia pipe formation that enhanced the permeability along the recrystallized limestone-schist contact and enabled incursions of cold oxygenated groundwater in the system.

The presence of Bi-sulfides speaks in favour of the skarn precursor for these types of fragments. Namely, according to fluid inclusion data published by STRMIĆ PALINKAŠ et al. (2013), the prograde skarn mineralization was formed at temperatures between 390 and 475°C. In contrast, the main ore deposition stage appears to have been largely contemporaneous with the retrograde stage of skarn development at temperatures below 350°C. In weakly acidic to near-neutral aqueous solutions Bi is predominantly transported as the $\mathrm{Bi(OH)_3^0}$ complex (SKIRROW & WALSHE, 2002) and its mobility is negligible at temperatures below 400°C (TOOTH et al., 2013).

The pyrite rim reflects sulfidation of magnetite into pyrite under the increased sulfur fugacity:

$$\mathrm{Fe^{2+}Fe^{3+}{}_2O_4} + 3\ \mathrm{S_2} + 8\ \mathrm{H^+} \rightarrow 3\ \mathrm{FeS_2} + 4\ \mathrm{H_2O} \quad (3)$$

magnetite *pyrite*

The isotope composition of sulfides from the Trepča Pb-Zn-Ag skarn deposit suggest a magmatic origin of sulfur (STRMIĆ PALINKAŠ et al., 2013). The solubility of sulfur in silicate magma is a function of temperature, pressure, FeO and $\mathrm{SiO_2}$ content and oxygen fugacity (CARROLL & WEBSTER, 1994; O'NEILL & MAVROGENES, 2002; DE MOOR et al., 2013). Under reducing conditions, the sulfur solubility decreases with decreasing temperature, and cooling of magma plays an important role in sulfur degassing. Furthermore, at the Trepča Pb-Zn-Ag skarn deposit, phreatomagmatic explosions and formation of diatreme unsealed the system, decreased the pressure and additionally favouring sulfur release.

P-T-X characteristics of fluids involved in retrograde alteration processes are evidenced by multiple generations of fluid inclusions. Primary liquid-rich fluid inclusion assemblages in calcite grains entrap moderate salinity high temperature fluids. A significant increase in salinity recorded by the coexisting primary liquid- and vapour-rich inclusions may have been caused by boiling within an open system (e.g. SIMMONS & BROWNE, 1997; BAUMGARTNER, 2008) and may not represent a fluid that originally had higher salinities. Alternatively, as reported by SIMMONS (1991) and ALBINSON et al. (2001) at the Fresnillo Pb-Zn-Ag deposit, Zacatecas, Mexico, the variation in salinity may have been caused by discrete pulses of saline fluids. The presence of numerous vapour-rich inclusions favours a boiling scenario that would also be consistent with the observed salinity variations without temperature change. Assuming hydrostatic conditions, boiling occurred at depths between 600 and 800 m (Fig. 11). The pseudosecondary liquid-rich fluid inclusion assemblages suggest dilution and cooling over time. Sporadic boiling episodes increased the salinity up to 0.3 wt.% NaCl (from 2.2-4.8 wt.% NaCl equ. up to 2.6-5.1 wt.% NaCl equ.) suggesting steam loss of between 6 and 15%. The decreased $\delta^{13}C$ and $\delta^{18}O$ values obtained for calcite grains suggest an involvement of magmatic $\mathrm{CO_2}$ (Table 3, Fig. 7). Similar $\delta^{13}C$ and $\delta^{18}O$ values have been recorded for the recrystallized limestone fragments as well as for the recrystallized limestone that hosts the skarn mineralization (Table 3, Fig. 7).

The fragments composed of pyrite, pyrrhotite and minor Bi-sulfides reflect that locally increases in sulfur fugacity were sufficient to complete sulfidation of hedenbergite to pyrrhotite and/or pyrite. Bismuth, a trace element in the skarn paragenesis, behaves in an immobile manner during the retrograde alteration processes accumulating in forms of various Bi-sulfides.

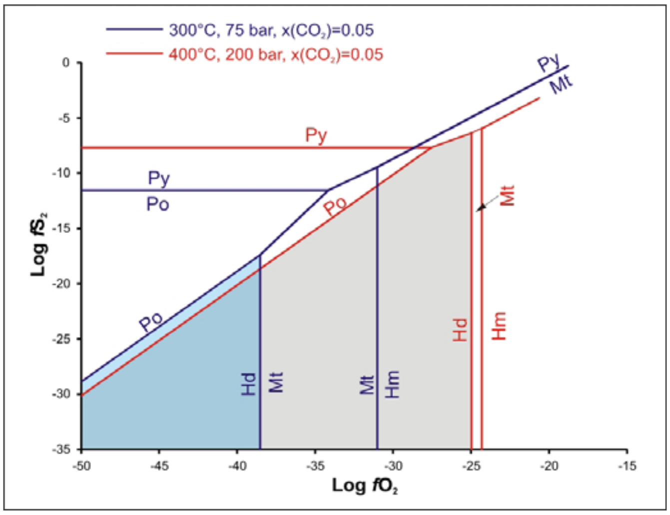

Figure 12. Log fO_2 vs. log fS_2 diagram of the Ca-Fe-Si-S-OH system constructed for the pre-breccia stage (lithostatic regime; P ≈ 20 MPa; T ≈ 400°C) and the main stage of the breccia formation (hydrostatic regime; P ≈ 7.5 MPa; T ≈ 300°C). The $x(CO_2)$ value is set at 0.05.

The limestone fragments found in the deeper portion of the breccia pipe are commonly replaced by siderite and occasionally impregnated by pyrite and microcrystalline quartz. Dickite aggregates and euhedral quartz occupy cavities. The fluid inclusion data obtained from quartz suggest a formation temperature of between 290 and 330ºC, from a fluid with salinity in the range of 6-8.5 wt% NaCl equ. and a pH below 5.5 (STRMIĆ PALINKAŠ et al., 2009). The $\delta^{34}S$ value of pyrite suggests a magmatic source of sulfur (STRMIĆ PALINKAŠ, 2009).

Two distinctive generations of fluid inclusions in recrystallized limestone fragments accompanied with fibroradial arsenopyrite and magnetite suggest the dilution and cooling of hydrothermal fluids over time. The $\delta^{13}C$ and $\delta^{18}O$ values overlap with data obtained for calcite hosted by fragments composed of a magnetite core and pyrite rim, the recrystallized limestone fragments and the recrystallized limestone that hosts the skarn mineralization (Table 3, Fig. 7).

5.6. HYDROTHERMAL CARBONATES

The recrystallized limestone that hosts the hydrothermal mineralization shows a weak contribution of magmatic CO_2 and slight enrichment in Mn and Fe. Concentration of other elements overlap with values obtained for the barren recrystallized Upper Triassic limestone.

Syn-ore and post-ore carbonates associated with both skarn and hydrothermal parageneses point to the diminishing influence of magmatic CO_2 during the main-ore and post-ore stages (Table 3, Fig. 7). Syn-ore carbonates are enriched in Fe, Mg, Mn, many chalcophile elements, including Ag, As, Bi, Cd, Cu, Pb, Sb and Zn, as well as in Au, Y and REE. Post-ore carbonates are depleted in Fe, Mg, Mn and the majority of chalcophile elements comparing to syn-ore carbonates, reflecting declining hydrothermal activity.

Traveritine, with traces of carbonates enriched in Zn and grains of galena, barite and gypsum, was precipitated during the late stage of hydrothermal activity. According to PENTECOST (2005), travertines are chemically-precipitated continental limestones where precipitation is mainly driven by CO_2 degassing from a groundwater source leading to calcium carbonate supersaturation. Based on the origin of the CO_2 interacting with the groundwater PENTECOST (2005) subdivided travertines into meteogene and thermogene deposits. Soil-zone and atmospheric CO_2 may be characterized as meteoric in origin, since the terrestrial vegetation and associated soil contains carbon fixed from the atmosphere. Travertines formed from groundwaters charged with a meteoric carrier are termed meteogene whereas thermogene travertines are formed as a massive deposit from fluids carrying CO_2 originating from thermal processes. Waters related to meteogene travertines have a lower temperature (generally ambient), a lower dissolved inorganic carbon content (DIC < 10 mmol/L), a lower CO_2 partial pressure ($pCO_2 < 0.01$ MPa) and pH values between 7 and 8. Furthermore, while meteogene travertines generally display a negative carbon isotope composition ($\delta^{13}C$ between -12 and 0‰), thermogene travertines, in contrast, show $\delta^{13}C$ values in the range of -1 to 10‰ (PENTECOST, 2005). On the basis of the geochemical characteristics the Trepča travertine should have been considered as thermogene in its origin although a contribution of organic-derived carbon cannot be excluded. Particularly, signs of rapid CO_2 degassing during deposition such as bubbles and radial calcite crystals are typical ofthermogene travertine. The $\delta^{13}C$ data mostly overlap with $\delta^{13}C$ values previously published for thermogene travertines with a magmatic origin of CO_2 (e.g. PENTECOST, 2005; D'ALESSANDRO et al., 2007). In addition, dissolution of the host recrystallized limestone during the main ore stage enriched hydrothermal fluids on HCO_3^-. Furthermore, decreased $\delta^{13}C$ values reflect the influence of organic carbon (e.g. LAZAREVA et al., 2008). The $\delta^{18}O$ value is predominantly affected by a significant contribution of circulating groundwaters at elevated temperatures.

5.7. PYROCLASTIC DEPOSITS

According to their isotope composition, calcite grains hosted by pyroclastic material of the caldera represent minute fragments of the recrystallized Triassic limestone. In contrast, the carbonate matrix is significantly depleted in ^{13}C reflecting the contribution of organic carbon. Textural characteristics of pyroclastic material with fossil imprints of leaves and plant roots evidence precipitation within a lacustrine environment enriched in organic matter remains. However, a contribution of magmatic CO_2 should not be ignored. Fluid inclusions hosted by calcite grains suggest their formation under boiling conditions. Homogenization temperatures between 320 and 340°C for fluid inclusions with salinities around 7 wt.% NaCl equ. indicate the formation depth of approximately 500 - 650 m and 1300 - 1750 m assuming lithostatic and hydrostatic conditions (Fig. 11), respectively. Younger V-rich inclusions reflect a sudden pressure drop probably related to phreatomagmatic explosions.

5.8. THE K/Ar AGE

The presence of the hydrothermally altered quartz-latite dyke within the main breccia core and overlapping K/Ar ages of hydrothermally altered quartz-latite (24.0 ± 0.7 Ma and 25.1 ± 0.9 Ma) and the milled matix breccia (23.2 ± 0.7 Ma) suggest that magmatic activity coincided with the mineralizing events. The volcanic rocks in the area, produced by the Late Oligocene postcollisional magmatic activity (CVETKOVIĆ et al., 2004), display mostly overlapping K/Ar (this study) and Ar/Ar ages (BOROJEVIĆ ŠOŠTARIĆ et al., 2012).

6. CONCLUSIONS

According to the mineralogical, geochemical and isotope data we can distinguish several stages that directed formation of the phreatomagmatic breccia pipe at the Trepča Pb-Zn-Ag skarn deposit:

1) The stage of isochemical contact metamorphism resulted from emplacement of a magmatic chamber during the Late Oligocene postcollisional magmatic activity. This stage preceded the mineralization and the breccia formation and resulted in the recrystallization of country rocks without significant changes in their chemical and isotope composition.

2) The stage of prograde (skarn) mineralization preceded the breccia formation. The prograde (skarn) mineralization resulted from the interaction of magmatic fluids with the recrystallized Upper Triassic limestone. The magmatic fluids were derived from a cooling magmatic body below the ore deposit. The host recrystallized limestone at the contact with the prograde (skarn) mineralization has an increased Fe, Mn, Mo, As, Au, Cs, Ga, REE and Y content suggesting their transport by infiltrating magmatic fluids. The decreased δ^{13}C and δ^{18}O values reflect the contribution of magmatic CO_2. In addition, the pyroxene predominant mineralogy reflects a low oxygen fugacity and a low water activity.

3) Emplacement of the quartz-latite dyke along the contact between the recrystallized limestone and the overlying schist. An interaction of the hot magmatic body with cold ground water resulted in phreatomagmatic explosions and formation of the phreatomagmatic breccia. The pyroclastic deposits found at the surface of the Trepča Pb-Zn-Ag skarn deposit confirm subaqueous explosive volcanic activity.

The contact between the main breccia pipe and the host recrystallized limestone has preserved geochemical and isotope evidence of variable P-T-X conditions during the phreatomagmatic brecciation. The early generations of fluid inclusions precede the brecciation and reflect the recrystallization under lithostatic conditions at temperatures between 350 and 370°C. The phreatomagmatic brecciation turned the system from the lithostatic to hydrostatic regime, decreasing the pressure and triggering the fluid boiling. Assuming an adiabatic process, the temperature drop from 350-370°C to 285-305°C resulted with a steam loss of approximately 30%. The later generations of fluid inclusions point to cooling and dilution of the fluids due to an enhanced contribution of descending groundwaters in late stages of the breccia formation. The host recrystallized limestone at the contact with the main breccia pipe is enriched in Si, Fe, Mn, Pb, As, Sb, W, REE and Y and depleted in ^{13}C and ^{18}O.

The lateral dyke-like branches infilled with the milled matrix represent non-venting branches of the main phreatomagmatic breccia. The fluid inclusions founded in the recrystallized limestone at contacts with the fissures indicate that hot (365-375°C) and moderate salinity single phase aqueous (liquid) fluids enriched in Pb, Ni, As, Cd and Sb were channeled through the fissures under lithostatic conditions.

4) The hydrothermally altered quartz-latite dyke points to an increase in water activity over time. Partly preserved sanidine accompanied with the mixture of muscovite and quartz reflects a near-neutral to weakly acidic environment.

5) The clasts of country rocks and skarn mineralization underwent intense milling and mixing due to repeated magmatic penetrations. Sericitization of the breccia matrix, locally accompanied with minor kaolinitization, point to an increased water activity under near-neutral to weakly acidic conditions. Large fragments originally composed of anhydrous skarn minerals (pyroxenes) are usually completely altered to a mixture of fibroradial magnetite, quartz and various amount of carbonates suggesting an increase in oxygen fugacity. Their pyrite rims reflect that the increase in the oxygen fugacity was followed by an increase in sulfur fugacity. The fragments predominantly composed of Fe-sulfides and minor Bi-sulfides indicate that locally increases in sulfur fugacity were sufficient to complete sulfidation of hedenbergite to pyrrhotite and/or pyrite. The increase in water activity and oxygen fugacity are associated with the breccia pipe formation that enhanced the permeability along the recrystallized limestone-schist contact and enabled groundwater incursions in the system. At the same time, cooling and decompression of the system intensified the magmatic sulfur degassing.

7) Syn-ore and post-ore carbonates associated with both skarn and hydrothermal parageneses reflect the diminishing influence of magmatic CO_2 during the main-ore and post-ore stages. Syn-ore carbonates are enriched in Fe, Mg, Mn, many chalcophile elements, including Ag, As, Bi, Cd, Cu, Pb, Sb and Zn, as well as in Au, Y and REE. In contrast, post-ore carbonates reflect a declining hydrothermal activity and the depletion in Fe, Mg, Mn and the majority of chalcophile elements.

8) Travertine deposits were precipitated in the late stage of hydrothermal activity at the Trepča Pb-Zn-Ag skarn deposit. Their isotope signature suggests that carbon originates predominantly from the dissolute host recrystallized limestone influenced by significant amounts of magmatic and organic carbon. In contrast, δ^{18}O values are strongly affected by the contribution of circulating groundwaters at elevated temperatures.

Although the phreatomagmatic breccia at the Trepča Pb-Zn-Ag skarn deposit does not carry significant amounts of the ore mineralization, its formation was crucial for ore deposition. Phreatomagmatic explosions and formation of the breccia triggered the retrograde stage increasing the water activity and oxygen fugacity in the system. In addition, cooling and decompression of the system contributed to more effective degassing of magmatic sulfur increasing the sulfur fugacity.

Acknowledgement

This study was supported by the Croatian Ministry of Sciences, Technology and Sports (Projects 119-0982709-1175). We are grateful to the geological teams of the Trepča deposit, in particular to M. DIEHL for help and constructive discussions during fieldwork. We would especially like to thank reviewers, Vasilios MELFOS and Irina MARINOVA, whose comments improved the paper.

REFERENCES

ALBINSON, T., NORMAN, D.I., COLE, D. & CHOMIAK, B. (2001): Controls on formation of low-sulfidation epithermal deposits in Mexico: Constraints from fluid inclusion and stable isotope data.– Society of Economic Geologist Special Publication, 8, 1–32.

ANDERSON, E.D., ATKINSON JR, W.W., MARSH, T. & IRIONDO, A. (2009): Geology and geochemistry of the Mammoth breccia pipe, Copper Creek mining district, southeastern Arizona: evidence for a magmatic–hydrothermal origin.– Miner. Deposita, 44/2, 151–170. doi: 10.1007/s00126-008-0206-2

BAKER, E.M., KIRWIN, D.J. & TAYLOR, R.G. (1986): Hydrothermal breccia pipes.– EGRU Contribution 12, James Cook University of North Queensland, Australia, 45p.

BAKER, E.M. & ANDREW, A.S. (1991): Geologic, fluid inclusion and stable isotope studies of the gold-bearing breccia pipe at Kidston, Queensland, Australia.– Econ. Geol., 86/4, 810-830. doi: 10.2113/gsecongeo.86.4.810

BALOGH, K. (1985): K/Ar dating of Neogene volcanic activity in Hungary: experimental technique, experiences and methods of chronological studies.– ATOMKI report, Debrecen, D/1, 277–288.

BAUMGARTNER, R., FONTBOTÉ, L. & VENNEMANN, T. (2008): Mineral zoning and geochemistry of epithermal polymetallic Zn-Pb-Ag-Cu-Bi mineralization at Cerro de Pasco, Peru.− Econ. Geol., 103/3, 493-537. doi: 10.2113/gsecongeo.103.3.493

BODNAR, R.J. (2003): Introduction to fluid inclusions.− Min Assoc Can Short Course Series, 32, 1–8.

BODNAR, R.J. & VITYK, M.O. (1994): Interpretation of microthermometric data for H_2O-NaCl fluid inclusions.– In: DE VIVO, B. & FREZZOTTI, M.L. (eds.): Fluid Inclusions in Minerals: Methods and Applications. Short Course of the Working Group (IMA) Inclusions in Minerals, Virginia Polytechnic Institute and State University, Blacksburg, Virginia, 117–130.

BODNAR, R.J., REYNOLDS, T.J. & KUEHN, C.A. (1985): Fluid inclusion systematics in epithermal systems.– Rev. Econ. Geol., 2, 73–98.

BORISENKO, A.S. (1977): Study of the salt composition of solutions of gas–liquid inclusions in minerals by the cryometric method.– Geol.Geofiz., 18, 16–27.

BOROJEVIĆ ŠOŠTARIĆ, S., CVETKOVIĆ, V., NEUBAUER, F., PALINKAŠ, L.A., BERNROIDER, M. & GENSER, J. (2012) Oligocene shoshonitic rocks of the RogoznaMts.(Central Balkan Peninsula): Evidence of petrogenetic links to the formation of Pb–Zn–Ag ore deposits.– Lithos, 148/1, 176–195.

BOROJEVIĆ ŠOŠTARIĆ, S., PALINKAŠ, L.A., NEUBAUER, F., HURAI, V., CVETKOVIĆ, V., ROLLER-LUTZ, Z., MANDIĆ, M. & GENSER, J. (2013): Silver-base metal epithermal vein and listwanite hosted deposit Crnac, Rogozna Mts., Kosovo, part II: A link between magmatic rocks and epithermal mineralization.– Ore Geol. Rev., 50/1, 98–117.

BOROJEVIĆ ŠOŠTARIĆ, S., PALINKAŠ, A.L., NEUBAUER, F., CVETKOVIĆ, V., BERNROIDER, M. & GENSER, J. (2014): The origin and age of the metamorphic sole from the Rogozna Mts., Western Vardar Belt: New evidence for the one-ocean model for the Balkan ophiolites.– Lithos, 192/1, 39–55.

BRANQUET, Y., CHEILLETZ, A., GIULIANI, G., LAUMONIER, B. & BLANCO, O. (1999): Fluidized hydrothermal breccia in dilatant faults during thrusting: the Colombian emerald deposits.– Geological Society, London, Special Publications, 155, 183–195. doi: 10.1144/GSL.SP.1999.155.01.14

BYRNE, K. & TOSDAL, R.M. (2014): Genesis of the Late Triassic southwest zone breccia-hosted alkalic porphyry Cu-Au deposit, Galore Creek, British Columbia, Canada.– Econ. Geol., 109/4, 915-938. doi: 10.2113/econgeo.109.4.915

CANET, C., GONZÁLEZ-PARTIDA, E., CAMPRUBÍ, A., CASTRO-MORA, J., ROMERO, F.M., PROL-LEDESMA, R.M., LINARES, C., ROMERO-GUADARRAMA, J.A. & SÁNCHEZ-VARGAS, L.I. (2011): The Zn–Pb–Ag skarns of Zacatepec, Northeastern Oaxaca, Mexico: A study of mineral assemblages and ore-forming fluids.– Ore Geol. Rev., 39/4, 277–290.

CANNELL, J., COOKE, D.R., WALSHE, J.L. & STEIN, H. (2005): Geology, mineralization, alteration, and structural evolution of the El Teniente porphyry Cu-Mo deposit.– Econ. Geol., 100/5, 979–1003. doi: 10.2113/gsecongeo.100.5.979

CARROLL, M.R. & WEBSTER, J.D. (1994): Solubilities of sulfur, noble gases, nitrogen, chlorine, and fluorine in magmas.– Rev. Miner. Geochem., 30, 231–279.

CLARK, C. & JAMES, P. (2003): Hydrothermal brecciation due to fluid pressure fluctuations: examples from the Olary Domain, South Australia.– Tectonophysics, 366/3, 187–206. doi: 10.1016/S0040-1951(03)00095-7

CLAYPOOL, G.E., HOLSER, W.T., KAPLAN, I.R., SAKAI, H. & ZAK, I. (1980): The age curves of sulfur and oxygen isotopes in marine sulfate, and their mutual interpretation.– Chem Geol, 28/1, 199–259. doi: 10.1016/0009-2541(80)90047-9

COOKE, D.R. & BLOOM, M.S. (1990): Epithermal and subjacent porphyry mineralization, Acupan, Baguio district, Philippines: a fluid-inclusion and paragenetic study.– J. Geochem.Explor., 35/1, 297–340. doi: 10.1016/0375-6742(90)90042-9

CORBETT, G.J. & LEACH, T.M. (1998): Southwest Pacific rim gold-copper systems: Structure, alteration, and mineralization.– Society of Economic Geologists Special Publication, 6, 234.

CVETKOVIĆ, V., KARAMATA, S. & KNEŽEVIĆ, V. (1995): Volcanic rocks of the Kopaonik District.– Geology and Metallogeny of the Kopaonik Mt. Symposium, Belgrade, 185–194.

CVETKOVIĆ, V., PRELEVIĆ, D., DOWNES, H., JOVANOVIĆ, M., VASELLI, O. & PECSKAY, Z. (2004): Origin and geodynamic significance of Tertiary postcollisional basaltic magmatism in Serbia (central Balkan Peninsula).– Lithos, 73/3–4, 161−186. doi: 10.1016/j.lithos.2003.12.004

D’ALESSANDRO, W., GIAMMANCO, S., BELLOMO, S. & PARELLO, F. (2007): Geochemistry and mineralogy of travertine deposits of the SW flank of Mt. Etna (Italy): Relationships with past volcanic and degassing activity.– J. Volcanol. Geoth. Res., 165/1−2, 64-70. doi: 10.1016/j.jvolgeores.2007.04.011

DAVIES, A.G., COOKE, D.R., GEMMELL, J.B. & SIMPSON, K.A. (2008): Diatreme breccias at the Kelian gold mine, Kalimantan, Indonesia: Precursors to epithermal gold mineralization.– Econ. Geol., 103/4, 689-716. doi: 10.2113/gsecongeo.103.4.689

DE MOOR, J.M., FISCHER, T.P., SHARP, Z.D., KING, P.L., WILKE, M., BOTCHARNIKOV, R.E., COTTRELL, E., ZELENSKI, M., MARTY, B., KLIMM, K., RIVARD, C., AYALEW, D., RAMIREZ, C. & KELLEY, K.A. (2013): Sulfur degassing at Erta Ale (Ethiopia) and Masaya (Nicaragua) volcanoes: Implications for degassing processes and oxygen fugacities of basaltic systems.– Geochem. Geophy. Geosy., 14/10, 4076-4108. doi: 10.1002/ggge.20255

DILEK, Y., FURNES, H. & SHALLO, M. (2007): Suprasubduction zone ophiolite formation along the periphery of Mesozoic Gondwana.– Gondwana Res., 11/4, 453–475. doi: 10.1016/j.gr.2007.01.005

DIMITRIJEVIĆ, M.D. (2001): The Dinarides and the Vardar zone: A short review of the geology.– Acta Vulcanol., 13/1, 1–8.

ELDERFIELD, H. & GREAVES, M.J. (1982): The rare earth elements in seawater.– Nature 296, 214–219. doi: 10.1038/296214a0

FÉRAUD, J., MALIQI, G. & MEHA, V. (2007): Famous mineral localities: the Trepca mine, Stari Trg, Kosovo.– Mineral. Rec., 38/4, 267–298.

GOLDSTEIN, R.H. (2001): Fluid inclusions in sedimentary and diagenetic systems.– Lithos, 55/1, 159–193. doi: 10.1016/S0024-4937(00)00044-X

GOLDSTEIN, R.H. & REYNOLDS, T.J. (1994): Systematics of fluid inclusions in diagenetic minerals.– Society for Sedimentary Geology, Short Course, 31, 199 p. doi: 10.2110/scn.94.31

HAAS, J.L. (1971): The effect of salinity on the maximum thermal gradient of a hydrothermal system at hydrostatic pressure.– Econ. Geol., 66/6, 940–946. doi: 10.2113/gsecongeo.66.6.940

HENLEY, R.W. (1984): Chemical structure of geothermal systems.– Rev. Econ. Geol., 1, 73–98.

HU, X., WANG, Y.L. & SCHMITT, R.A. (1988): Geochemistry of sediments on the Rio Grande Rise and the redox evolution of the south Atlantic Ocean.– Geochim. Cosmochim. Acta, 52, 201–207. doi: 10.1016/0016-7037(88)90068-3

JAEGER, J.C. & COOK, N.G.W. (1979): Fundamentals of rock mechanics.– Chapman and Hall, London, 593 p.

JANKOVIĆ, S. (1997): The Carpatho-Balkanides and adjacent area: A sector of the Tethyan Eurasian metallogenic belt.– Miner. Deposita, 32/5, 426–433.

KARAMATA, S., MAJER, V. & PAMIĆ, J. (1980): Ophiolites of Yugoslavia.– Ofioliti, 1/1, 105–125.

KARAMATA, S., OLUJIĆ, J., PROTIĆ, LJ., MILOVANOVIĆ, D., VUJNOVIĆ, L., POPEVIĆ, A., MEMOVIĆ, E., RADOVANOVIĆ, Z. & RESIMIĆ-ŠARIĆ, K.(2000): The Western belt of the Vardar zone the remnant of a marginal sea.– In: KARAMATA, S. & JANKOVIĆ, S. (eds.): Geology and metallogeny of the Dinarides and the Vardar zone: Zvornik, Academy of Science and Arts of Republika Srpska, 131–135.

KEENAN, J.H., KEYES, F.G., HILL, P.G. & MOORE, J.G. (1969): Steam Tables.– John Wiley, New York, 1962 p.

KOŁODZIEJCZYK, J., PRŠEK, J., MELFOS, V., VOUDOURIS, P.C., MALIQI, F. & KOZUB-BUDZYŃ, G. (2015): Bismuth minerals from the StanTerg deposit (Trepça, Kosovo).– Neues Jb. Miner. Abh., 192/3, 317–333.

LANDTWING, M.R., DILLENBECK, E.D., LEAKE, M.H. & HEINRICH, C.A. (2002): Evolution of the breccia-hosted porphyry Cu-Mo-Au deposit at Agua Rica, Argentina: Progressive unroofing of a magmatic hydrothermal system.– Econ. Geol., 97/6, 1273−1292. doi: 10.2113/gsecongeo.97.6.1273

LAZAREVA, E.V., BRYANSKAYA, A.V., ZHMODIK, S.M., PONOMARCHUK, V.A., BARKHUTOVA, D.D. & SEMIONOVA, D.V. (2008): Carbon isotope composition in microbial mats and travertine of BRZ.– Geochim.Cosmochim.Acta, 72/12, A521.

LORENZ, V. (1973): On the formation of maars.– Bull.Volcanol., 37/2, 183–204. doi: 10.1007/BF02597130

MALO, M., MORITZ, R., DUBE, B., CHAGNON, A., ROY, F. & PELCHAT, C. (2000): Base metal skarns and Au occurrences in the southern Gaspé Appalachians: distal products of a faulted and displaced magmatic-hydrothermal system along the Grand Pabos-Restigouche fault system.– Econ. Geol., 95/6, 1297–1318.

McCALLUM, M.E. (1985): Experimental evidence for fluidization processes in breccia pipe formation.– Econ. Geol., 80/6, 1523–1543. doi: 10.2113/gsecongeo.80.6.1523

MEINERT, L.D. (1992): Skarns and skarn deposits.– Geosci. Can., 19/4, 145–162.

MEINERT, L.D., DIPPLE, G.M. & NICOLESCU, S. (2005): World skarn deposits.– Econ. Geol. 100th Anniversary Volume, 299–336.

MILOVANOVIĆ, D., MARCHIG, V. & KARAMATA, S. (1995): Petrology of the crossite schist from Fruška Gora Mts. (Yugoslavia), relic of a subducted slab of the Tethyan oceanic crust.– J. Geodyn., 20/3, 289–304.

NANCE, W.B. & TAYLOR, S.R. (1976): Rare earth element patterns and crustal evolution: I. Australian post-Archean rocks.– Geochim. Cosmochim. Acta, 40/12, 1539−1551. doi: 10.1016/0016-7037(76)90093-4

PENTECOST, A. (2005): Travertine.– Springer-Verlag, Berlin Heidelberg, 445 p.

ROBERTSON, A.H., TRIVIĆ, B., ĐERIĆ, N. & BUCUR, I.I. (2013): Tectonic development of the Vardar ocean and its margins: Evidence from the Republic of Macedonia and Greek Macedonia.– Tectonophysics, 595/1, 25–54. doi: 10.1016/j.tecto.2012.07.022

ROSATELLI, G., WALL, F., STOPPA, F. & BRILLI, M. (2010): Geochemical distinctions between igneous carbonate, calcite cements, and limestone xenoliths (Polino carbonatite, Italy): spatially resolved LAICPMS analyses.– Contrib. Mineral. Petr., 160/5, 645-661. doi: 10.1007/s00410-010-0499-x

SAMSON, I.M. & WALKER, R.T. (2000): Cryogenic Raman spectroscopic studies in the system $NaCl–CaCl_2–H_2O$ and implications for low-temperature phase behaviour in aqueous fluid inclusions.– Can. Mineral., 38/1, 35–43.

SCHUMACHER, F. (1950): Die Lagerstätte der Trepča und ihre Umgebung.- Izdavačko Preduzeće Saveta za Energetiku i Ekstraktivnu Industriju vlade FNRJ, Beograd, 65 p.

SCHUMACHER, F. (1954): The ore deposits of Yugoslavia and the development of its mining industry.– Econ. Geol., 49/5, 451–492.

SHARP, I.R. & ROBERTSON, A.H. (2006): Tectonic-sedimentary evolution of the western margin of the Mesozoic Vardar Ocean: evidence from the Pelagonian and Almopias zones, northern Greece.– Geological Society, London, Special Publications, 260/1, 373–412. doi: 10.1144/GSL.SP.2006.260.01.16

SILLITOE, R.H. (1985): Ore-related breccias in volcanoplutonic arcs.– Econ. Geol., 80/6, 1467–1514. doi: 10.2113/gsecongeo.80.6.1467

SILLITOE, R.H., BAKER, E.M. & BROOK, W.A. (1984): Gold deposits and hydrothermal eruption breccias associated with a maar volcano at Wau, Papua New Guinea.– Econ. Geol., 79/4, 638-655. doi: 10.2113/gsecongeo.79.4.638

SIMMONS, S.F. (1991): Hydrologic implications of alteration and fluid inclusion studies in the Fresnillo district, Mexico: Evidence for a brine reservoir and a descending water table during the formation of hydrothermal Ag-Pb-Zn orebodies.– Econ. Geol., 86/8, 1579–1601. doi: 10.2113/gsecongeo.86.8.1579

SIMMONS, S.F. & BROWNE, P.R.L. (1997): Saline fluid inclusions in sphalerite from the Broadlands-Ohaaki geothermal system: A coincidental trapping of fluids being boiled toward dryness.– Econ. Geol., 92/4, 485–489. doi: 10.2113/gsecongeo.92.4.485

SIMPSON M.P., STRMIĆ PALINKAŠ S., MAUK J.L., BODNAR R.J. (2015): Fluid inclusion chemistry of adularia-sericite epithermal Au-Ag deposits of the southern Hauraki Goldfield, New Zealand.– Econ. Geol., 110/3, 763–786.

SKEWES, M.A., HOLMGREN, C. & STERN, C.R. (2003): The Donoso copper-rich, tourmaline-bearing breccia pipe in central Chile: petrologic, fluid inclusion and stable isotope evidence for an origin from magmatic fluids.– Miner. Deposita, 38/1, 2–21. doi: 10.1007/s00126-002-0264-9

SKIRROW, R.G. & WALSHE, J.L. (2002): Reduced and oxidized Au-Cu-Bi iron oxide deposits of the Tennant Creek Inlier, Australia: An integrated geologic and chemical model.– Econ. Geol., 97/6, 1167−1202. doi: 10.2113/gsecongeo.97.6.1167

STERNER, S.M., HALL, D.L. & BODNAR, R.J. (1988): Synthetic fluid inclusions. V. Solubility relations in the system $NaCl-KCl-H_2O$ under vapor-saturated conditions.– Geochim. Cosmochim. Acta, 52/5, 989–1005. doi: 10.1016/0016-7037(88)90254-2

STRMIĆ PALINKAŠ, S. (2009): Genesis of hydrothermal and skarn paragenesis in the Pb-Zn-Ag mineral deposit Trepča (StariTrg), Kosovo.– Unpublished PhD thesis, University of Zagreb, Zagreb, 143 p.

STRMIĆ PALINKAŠ, S., PALINKAŠ, L.A., MOLNAR, F. & DIEHL, M. (2007): Basic research in service of successful exploitation in Pb-Zn-Ag Stari Trg mine, Trepča, Kosovo.– In: ANDREW, C.J. (ed.): Digging deeper: Navan, Ireland, Irish Association for Economic Geology, 165–167.

STRMIĆ PALINKAŠ, S., BOROJEVIĆ ŠOŠTARIĆ, S., BERMANEC, V., PALINKAŠ, L., PROCHASKA, W., FURIĆ, K. & SMAJLOVIĆ, J. (2009): Dickite and kaolinite in the Pb-Zn-Ag sulphide deposits of northern Kosovo (Trepča and Crnac).– Clay Miner., 44/1, 67–79.

STRMIĆ PALINKAŠ, S., PALINKAŠ, L.A., RENAC, C., SPANGENBERG, J.E., LÜDERS, V., MOLNAR, F. & MALIQI, G. (2013): Metallogenic model of the Trepča Pb-Zn-Ag skarn deposit, Kosovo: evidence from fluid inclusions, rare earth elements, and stable isotope data.– Econ. Geol., 108/1, 135–162.

STRMIĆ PALINKAŠ, S., WEGNER, R., ČOBIĆ, A., PALINKAŠ, L.A., DE BRITO BARRETO, S., VÁCZI, T. & BERMANEC, V. (2014): The role of magmatic and hydrothermal processes in the evolution of Be-bearing pegmatites: Evidence from beryl and its breakdown products.– Am. Mineral., 99/2-3, 424–432.

SUDAR, M. (1986):Mikrofosili I biostratigrafija trijasaunutrašnjih Dinarida između Gučeva I Ljubišnje (Triassic microfossils and biostratigraphy of the Inner Dinarides between Gučevo and Ljubišnja Mts., Yugoslavia; in Serbian with English summary).– Geol. An. Balk.Poluos., 50, 151–394.

SUDAR, M. & KOVACS, S. (2006): Metamorphosed and ductilely deformed conodonts from Triassic limestones situated beneath ophiolite complexes: Kopaonik Mountain (Serbia) and Bükk Mountains (NE Hungary)-a preliminary comparison.– Geol.Carpath., 57/3, 157−176.

TAMAS, C.G. & MILESI, J.-P. (2002): Hydrovolcanic breccia pipe structures-General features and genetic criteria. I. Phreatomagmatic breccias.– Studia UBB Geologia, 47/1, 127–147.

TERZIĆ, S.B., SOMMERAUER, J. &HARNIK, A.B. (1974): Macroscopic cosalite crystals from the Pb-Zn ore deposit Trepča (Yugoslavia).– Schweiz. Mineral. Petrogr. Mitt., 54/1, 209–211.

TOOTH, B., ETSCHMANN, B., POKROVSKI, G.S., TESTEMALE, D., HAZEMANN, J.-L., GRUNDLER, P.V. & BRUGGER, J. (2013): Bismuth speciation in hydrothermal fluids: An X-ray absorption spectroscopy and solubility study.– Geochim. Cosmochim. Acta, 101/1, 156–172. doi: 10.1016/j.gca.2012.10.020

TORNOS, F., CASQUET, C., GALINDO, C., VELASCO, F. & CANALES, A. (2001): A new style of Ni-Cu mineralization related to magmatic breccia pipes in a transpressional magmatic arc, Aguablanca, Spain.– Miner. Deposita, 36/7, 700–706. doi: 10.1007/s001260100204

TRUMBULL, R.B., SLACK, J.F., KRIENITZ, M.S., BELKIN, H.E. & WIEDENBECK, M. (2011): Fluid sources and metallogenesis in the Blackbird Co–Cu–Au–Bi–Y–REE district, Idaho, USA: insights from major-element and boron isotopic compositions of tourmaline.– Can. Mineral., 49/1, 225−244.

VASKOVIĆ, N. & MATOVIĆ, V. (2010): Ophiolites of the Vardar Zone and the Dinarides: Central and West Serbia.– IMA 2010 field trip guide RS1. Department of Mineralogy, Geochemistry and Petrology, University of Szeged, 55 p.

VEIZER, J.D. & HOEFS, J. (1976): The nature of $^{18}O/^{16}O$ and $^{13}C/^{12}C$ secular trends in sedimentary carbonate rocks.– Geochim. Cosmochim. Acta, 40/11, 1387–1395.

VESELINOVIC-WILLIAMS, M. (2011): Characteristics and origin of polymetallic mineralisation in the Kopaonik region of Serbia and Kosovo, with particular reference to the Belo Brdo Pb-Zn (Ag) deposit.– Unpublished PhD thesis, Kingston University, London, 150 p.

VRY, V.H., WILKINSON, J.J., SEGUEL, J. & MILLÁN, J. (2010): Multistage intrusion, brecciation, and veining at El Teniente, Chile: Evolution of a nested porphyry system.– Econ. Geol., 105/1, 119–153. doi: 10.2113/gsecongeo.105.1.119

WALLIER S, REY R, KOUZMANOV K, PETTKE T, HEINRICH CA, LEARY S, O'CONNOR G, TĂMAŞ CG, VENNEMANN T, ULLRICH T (2006): Magmatic fluids in the breccia-hosted epithermal Au-Ag deposit of Roşia Montană, Romania.– Econ. Geol., 101/5, 923–954.

YANG, K.& BODNAR, R.J. (1994): Why is economic porphyry copper mineralization absent from the granitoids of the Gyeongsang Basin, South Korea? Evidence from silicate melt and aqueous fluid inclusions.– Int. Geol. Rev., 36/7, 608–628.

ZELIĆ, M., AGOSTINI, S., MARRONI, M., PANDOLFI, L. & TONARINI, S. (2010): Geological and geochemical features of the Kopaonik intrusive complex (Vardar zone, Serbia).– Ofioliti, 35/1, 33–47.

ZHENG, Y.F. (1999): Oxygen isotope fractionation in carbonate and sulfate minerals.– Geochem. J., 33, 109–126. doi: 10.2343/geochemj.33.109

ZHENG, Y.F. & HOEFS, J. (1993): Carbon and oxygen isotopic covariations in hydrothermal calcites.– Miner. Deposita, 28/2, 79–89. doi: 10.1007/BF00196332